A&A 564, A55 (2014)
DOI: 10.1051/0004-6361/201323016

Astronomy & Astrophysics

New constraints on the formation and settling of dust in the atmospheres of young M and L dwarfs⋆,⋆⋆,⋆⋆⋆

E. Manjavacas[1], M. Bonnefoy[1,2], J. E. Schlieder[1], F. Allard[3], P. Rojo[4], B. Goldman[1], G. Chauvin[2], D. Homeier[3], N. Lodieu[5,6], and T. Henning[1]

[1] Max Planck Institute für Astronomie, Königstuhl 17, 69117 Heidelberg, Germany
e-mail: manjavacas@mpia.de
[2] UJF-Grenoble1/CNRS-INSU, Institut de Planétologie et d'Astrophysique de Grenoble (IPAG) UMR5274, Grenoble 38041, France
[3] CRAL-ENS, 46 allée d'Italie, 69364 Lyon Cedex 07, France
[4] Departamento de Astronomía, Universidad de Chile, Casilla 36-D, Santiago, Chile
[5] Instituto de Astrofísica de Canarias (IAC), Vía Láctea s/n, 38206 La Laguna, Tenerife, Spain
[6] Departamento de Astrofísica, Universidad de La Laguna (ULL), 38205 La Laguna, Tenerife, Spain

Received 8 November 2013 / Accepted 6 February 2014

ABSTRACT

Context. Gravity modifies the spectral features of young brown dwarfs (BDs). A proper characterization of these objects is crucial for the identification of the least massive and latest-type objects in star-forming regions, and to explain the origin(s) of the peculiar spectrophotometric properties of young directly imaged extrasolar planets and BD companions.
Aims. We obtained medium-resolution ($R \sim 1500-1700$) near-infrared (1.1−2.5 μm) spectra of seven young M9.5–L3 dwarfs classified at optical wavelengths. We aim to empirically confirm the low surface gravity of the objects in the near-infrared. We also test whether self-consistent atmospheric models correctly represent the formation and the settling of dust clouds in the atmosphere of young late-M and L dwarfs.
Methods. We used the Infrared Spectrometer And Array Camera (ISAAC) at the Very Large Telescope (VLT) to obtain the spectra of the targets. We compared the spectra to those of mature and young BDs, and to young late-type companions to nearby stars with known ages to identify and study gravity-sensitive features. We computed spectral indices weakly sensitive to the surface gravity to derive near-infrared spectral types. Finally, we found the best fit between each spectrum and synthetic spectra from the BT-Settl 2010 and 2013 atmospheric models. Using the best fit, we derived the atmospheric parameters of the objects and identified which spectral characteristics the models do not reproduce.
Results. We confirmed that our objects are young BDs and we found near-infrared spectral types in agreement with the ones determined at optical wavelengths. The spectrum of the L2γ dwarf 2MASSJ232252.99-615127.5 reproduces the spectrum of the planetary mass companion 1RXS J160929.1-210524b well. The BT-Settl models fit the spectra and the 1−5 μm spectral energy distribution of the L0–L3 dwarfs for temperatures between 1600−2000 K. But the models fail to reproduce the shape of the H band and the near-infrared slope of some of our targets. This fact, and the best-fit solutions found with super-solar metallicity, are indicative of a lack of dust, in particular at high altitude, in the cloud models.
Conclusions. The modeling of the vertical mixing and of the grain growth will be revised in the next version of the BT-Settl models. These revisions may suppress the remaining non-reproducibilities. Our spectra provide additional templates for the characterization of the numerous young L-type companions that will be detected in the coming years by planet imaging instruments such as VLT/SPHERE, Gemini/GPI, *Subaru*/SCexAO, and LBTI/LMIRCam.

Key words. stars: low-mass – brown dwarfs – planetary systems – techniques: spectroscopic

1. Introduction

Since the discovery of the first substellar objects (Nakajima et al. 1995; Rebolo et al. 1995), large infrared (IR) surveys have unearthed hundreds of brown dwarfs (BDs) in the field and in star forming regions. The spectral energy distributions of BDs peak in the infrared. Their spectra are dominated by broad, overlapping condensate and molecular absorption features (see Kirkpatrick 2005). The strength of these features depends on a combination of photospheric temperature, gas, pressure, and dust properties, which in turn are related to the effective temperature ($T_{\rm eff}$), surface gravity (g), and metallicity of the objects. Spectroscopic studies of mature (≫400 Myr) field BDs led to the definition of the spectral classes "L" (Kirkpatrick et al. 1999; Martín et al. 1999) for objects dominated by H_2O, FeH, and CO absorption bands in the near-infrared (NIR), and "T" (Burgasser et al. 2002; Geballe et al. 2002) for objects that exhibit strong CH_4+H_2O bands and collision-induced absorption (CIA) due to the presence of H_2 at these wavelengths. The change in the spectral morphology, used for the classification, is mostly tied to changes in $T_{\rm eff}$ (e.g., Testi 2009).

Substellar objects contract and cool down with time (Burrows et al. 1997; Baraffe et al. 1998). Therefore, young

⋆ Based on observations made with ESO telescopes at the Paranal Observatory under programs 085.C-0676 and 290.C-5145.
⋆⋆ Appendices are available in electronic form at http://www.aanda.org
⋆⋆⋆ The spectra (FITS files) are only available at the CDS via anonymous ftp to cdsarc.u-strasbg.fr (130.79.128.5) or via http://cdsarc.u-strasbg.fr/viz-bin/qcat?J/A+A/564/A55

objects can have larger radii and higher luminosities than older and more massive objects despite an identical effective temperature. The lower surface gravity of young objects ($g \propto M/R^2$) can be directly accessed by observation and can be used to break the degeneracy. Low surface gravity results in peculiar spectral characteristics such as the triangular H band shape in the NIR (Zapatero Osorio et al. 2000; Lucas et al. 2001) and reduced alkali lines in the optical and NIR (e.g., McGovern et al. 2004; Cruz et al. 2009). These modifications have nonetheless mostly been investigated for objects earlier than ~L4 found in young clusters and star forming regions (e.g., Luhman et al. 1997, 2004; Luhman 1999, 2004; Lucas et al. 2001; Martín et al. 2004; McGovern et al. 2004; Lodieu et al. 2008; Weights et al. 2009; Alves de Oliveira et al. 2012).

Advances in high-contrast and high-resolution imaging in the NIR (1–5 μm) led to the discovery of late-type companions to young nearby stars straddling the planet/BD boundary (e.g., Chauvin et al. 2004, 2005; Lafrenière et al. 2008; Marois et al. 2008, 2010; Lagrange et al. 2010; Ireland et al. 2011; Delorme et al. 2013; Rameau et al. 2013; Kuzuhara et al. 2013; Currie et al. 2014). Most of these objects have estimated effective temperatures similar to those of L dwarfs. The low- to medium-resolution ($R \leq 5000$) spectra and infrared photometry of these objects exhibit peculiar features (red pseudocontinua, triangular H band shape, lack of methane absorption, reduced K I and Na I lines; Lafrenière et al. 2008; Bonnefoy et al. 2010, 2014a; Patience et al. 2010; Wahhaj et al. 2011; Barman et al. 2011a; Oppenheimer et al. 2013). These peculiarities are likely directly related to the expected low surface gravity of the objects.

Nevertheless, the currently limited sample of young late-type objects with high signal-to-noise (S/N) spectra make the establishment of a proper empirical classification scheme challenging for these objects. Cruz et al. (2009) have identified a population of young bright and nearby L dwarfs isolated in the field. They developed a classification scheme in the optical. This scheme has been extended in the NIR for young L dwarfs by Bonnefoy et al. (2014a) and Allers & Liu (2013). Several of these peculiar L-type dwarfs share similarities with the spectra of young companions at these wavelengths (Bonnefoy et al. 2010, 2014a; Allers & Liu 2013; Faherty et al. 2013; Liu et al. 2013). Obtaining more NIR spectra of young isolated objects are therefore needed to consolidate the classification scheme and to identify further analogues to directly imaged exoplanets.

Atmospheric models allow us to disentangle the effect of varying $T_{\rm eff}$, log g, and (metallicity) M/H on the spectral features. Below $T_{\rm eff} \sim 2600$ K, models predict that clouds of iron and silicate grains begin to form, changing the opacity (Lunine et al. 1986; Tsuji et al. 1996; Burrows & Sharp 1999; Lodders 1999; Marley 2000; Marley & Ackerman 2001; Allard et al. 2001). The formation and the gravitational sedimentation of these dust clouds are influenced by the surface gravity. Dust cloud formation is expected to be more efficient at low gravity because the atmosphere is more extended and the gas is cooler. Low gravity tends to make the convection and the resulting mixing more efficient as well.

Modeling of the spectrophotometric data on young L and early-T type companions with parametrized models (Marley & Ackerman 2001; Burrows et al. 2001) has revealed anomalously thick clouds (Barman et al. 2011a,b; Skemer et al. 2012; Marley et al. 2013). These peculiar cloud properties may explain why some companions are "underluminous" in some bands (Skemer et al. 2012; Marley et al. 2012). Self-consistent atmospheric models, such as the BT-Settl models (Allard et al. 2013) and the Drift-PHOENIX models, (Helling et al. 2008), use cloud models where the dust properties do not require the definition of any other additional free parameters other than log g, $T_{\rm eff}$, M/H. Synthetic spectra for a specific set of atmospheric parameters can be compared to empirical spectra. These models are just starting to be tested on spectra of young late-type objects (companions and free-floating objects; Bonnefoy et al. 2010, 2014a; Witte et al. 2011; Patience et al. 2012). We used them on spectra of young M5.5–L0 dwarfs in Bonnefoy et al. (2014a) to reveal a drop of the effective temperature at the M/L transition. We suggested that this drop could be induced by an improper handling of the formation of dust clouds at the M/L transition in the models. The test however could not be extended to later spectral types and lower effective temperatures due to the lack of a consistent sample of young objects in the L dwarf regime at that time.

In this paper, we present a homogeneous set of seven medium-resolution ($R \sim 1500-1700$) spectra of M9.5–L3 dwarfs, all classified at optical wavelengths. Our sample is composed of the M9.5 object DENIS-P J124514.1-442907 (also called TWA 29; hereafter DENIS J1245) a member of TW-Hydrae (5–10 Myr), and the L0 dwarf Cha J1305-7739 (Jayawardhana & Ivanov 2006, hereafter Cha 1305), one of the least massive objects of the Chameleon II cluster. We also present the spectra of five L dwarfs with features indicative of low surface gravity (Lγ dwarfs) in the optical, identified by Cruz et al. (2009). These objects are the two L0γ dwarfs EROS J0032-4405 (Goldman et al. 1999, hereafter EROS J0032) and 2MASS J22134491-2136079 (Cruz et al. 2009, hereafter 2M2213), the L2γ dwarf 2MASSJ232252.99-615127.5 (Cruz et al. 2009, hereafter 2M2322), and the two L3γ dwarfs 2MASS J212650.40-814029.3 (Cruz et al. 2009, 2M2126) and 2MASSJ220813.63+292121.5 (Cruz et al. 2009, hereafter 2M2208).

We aim to use the spectra to confirm the low surface gravities of the objects in the NIR and to test the ability of the BT-Settl models to correctly handle the formation and gravitational settling of dust under reduced surface gravity conditions. These spectra enrich the scarce sample of empirical NIR medium-resolution spectra of young late-type objects beyond the M–L transition, especially for spectral type L3. We describe our observations and the associated data reduction in Sect. 2. We present an empirical analysis of the spectral features in order to derive NIR spectral types and confirm the young age of our targets in Sect. 3. In Sect. 4, we describe the comparison of the atmospheric models to the observed spectra. We discuss these comparisons and derive updated target properties in Sect. 5.

2. Observations and data reduction

Our targets were observed with the Infrared Spectrometer And Array Camera (ISAAC, Moorwood et al. 1998) mounted on the Very Large Telescope (VLT) ath the UT3 telescope. The instrument was operated in low-resolution mode with the 0.3″ slit at central wavelengths 1.25 μm, 1.65 μm, and 2.2 μm. This setup provides spectra with resolving powers of ~1700, 1600, and 1500 from 1.1–1.4 μm (J band), 1.42–1.82 μm (H band), and 1.82–2.5 μm (K band). Nodding and small jittering of the source along the slit were performed to correct bad pixels and to subtract the sky and bias contributions. Sources at high airmasses were observed with the slit aligned with the parallactic angle to mitigate differential flux losses.

We observed DENIS 1245 on 6 and 21 April 2010. We took 6×120 s exposures in the J band, and 6×90 s exposures in

Table 1. Observing log: λ_{ref} is the central wavelength of the band.

Name	Date	λ_{ref} (μm)	DIT (s)	NINT	Seeing ($''$)	Airmass	Notes
DENISJ1245	April 4, 2010	1.25	120	6	1.30	1.20	
DENISJ1245	April 21, 2010	1.25	120	6	0.80	1.07	
DENISJ1245	April 21, 2010	1.65	90	6	0.70	1.06	
DENISJ1245	April 21, 2010	2.20	90	6	0.55	1.06	
HIP 064550	April 4, 2010	1.25	5	2	1.15	1.20	G1.5V telluric standard
HIP 055667	April 21, 2010	1.25	5	2	0.70	1.07	B2IV-V telluric standard
HIP 055667	April 21, 2010	1.65	5	2	0.70	1.07	B2IV-V telluric standard
HIP 055667	April 21, 2010	2.20	5	2	0.60	1.07	B2IV-V telluric standard
EROS J0032	July 6, 2010	1.25	180	6	1.30	1.07	
EROS J0032	July 15, 2010	1.65	120	6	0.85	1.07	
EROS J0032	July 15, 2010	2.20	120	6	0.85	1.07	
EROS J0032	July 25, 2010	1.25	180	6	0.70	1.10	
HIP 004722	July 6, 2010	1.25	5	2	–	1.08	G3V telluric standard
HIP 111085	July 15, 2010	1.65	5	2	1.02	1.16	B9V telluric standard
HIP 111085	July 15, 2010	2.20	5	2	1.04	1.16	B9V telluric standard
HIP 003356	July 25, 2010	1.25	5	2	0.80	1.07	B9.5V telluric standard
Cha 1305	April 6, 2010	1.65	200	6	0.90	1.90	
Cha 1305	April 21, 2010	1.25	240	8	0.60	1.67	
Cha 1305	April 21, 2010	1.65	200	6	0.50	1.66	
Cha 1305	April 21, 2010	2.20	180	10	0.80	1.70	
HIP 059830	April 6, 2010	1.65	5	2	0.80	1.97	B3V telluric standard
HIP 072671	April 21, 2010	1.25	5	2	–	1.60	B8V telluric standard
HIP 072671	April 21, 2010	1.65	5	2	0.59	1.56	B8V telluric standard
HIP 072671	April 21, 2010	2.20	5	2	0.75	1.56	B8V telluric standard
2M2322	June 9, 2010	1.25	240	6	1.00	1.35	
2M2322	June 9, 2010	1.65	120	10	0.80	1.28	
2M2322	June 9, 2010	2.20	120	10	1.00	1.26	
HIP 117661	June 9, 2010	1.25	5	2	0.70	1.40	B9V telluric standard
HIP 117661	June 9, 2010	1.65	5	2	0.90	1.39	B9V telluric standard
HIP 117661	June 9, 2010	2.20	5	2	1.00	1.33	B9V telluric standard
2M2126	April 21, 2010	1.65	180	6	0.60	2.02	
2M2126	April 21, 2010	2.20	180	4	0.60	1.99	
2M2126	June 7, 2010	1.25	180	12	0.90	1.84	
HIP 112781	April 21, 2010	1.65	5	2	1.10	2.08	B6IV telluric standard
HIP 112781	April 21, 2010	2.20	5	2	0.80	2.03	B6IV telluric standard
HIP 099400	June 7, 2010	1.25	5	2	0.80	1.73	B2IV telluric standard
2M2208	June 9, 2010	1.25	180	12	0.80	1.90	
2M2208	June 7, 2010	1.65	180	6	0.80	1.70	
2M2208	June 7, 2010	2.20	180	9	0.90	1.72	
HIP 112235	June 9, 2010	1.25	5	2	0.70	1.97	B9V telluric standard
HIP 112235	June 7, 2010	1.65	5	2	0.95	1.73	B9V telluric standard
HIP 112235	June 7, 2010	2.20	5	2	0.80	1.74	B9V telluric standard
2M2213	August 6, 2013	1.25	180	8	2.07	1.10	
2M2213	August 6, 2013	1.65	110	2	1.97	1.21	
2M2213	August 6, 2013	2.20	150	2	...	1.22	
HIP 114656	August 6, 2013	1.25	5	2	2.27	1.04	B9V telluric standard
HIP 114656	August 6, 2013	1.65	5	2	1.71	1.05	B9V telluric standard
HIP 114656	August 6, 2013	2.20	5	4	...	1.11	B9V telluric standard

Notes. DIT is the integration time in each position of the slit, and NDIT is the number of exposures.

the H and K bands. We moved the star along the slit between two positions separated by 20 arcsec following an ABBA strategy. We applied additional small offsets ($5''$) around the two source positions between each exposure to efficiently filter out nonlinear and hotpixels at the data reduction step. We followed a similar strategy for the remaining targets. Data integration times and the number of exposures are reported in Table 1. Early-type stars were observed soon after the science target at similar airmass to ensure a proper removal of telluric features. These observations are also summarized in Table 1. Calibrations were obtained during the day following the observations: flat fields, wavelength calibration frames, and frames with a star moving along the slit in low- and medium-resolution to compute the spectral curvature.

Data were reduced using the 6.1.3 version of the ISAAC pipeline (Devillard et al. 1999; Silva & Peron 2004) provided by the European Southern Observatory. The pipeline identifies pairs of sky-object frames and subtracts them. The calibration in wavelength and the slit curvature distortion were performed using exposures with the xenon and argon lamps. The slit curvature was modeled with a bivariate 2D polynomial. The dispersion relation was computed by matching a xenon and/or argon atlas with the corrected spectra. The pipeline divides the raw images by the flat field, corrects for bad pixels and distortion, and re-

constructs the combined sky-subtracted 2D spectra from a shift of the nodded images. The object flux is extracted in each spectral channel to build the final spectrum.

Data on the objects and associated telluric standard stars were reduced in a similar way. Telluric standard star spectra were divided by a blackbody with a temperature that corresponded to their spectral type (Theodossiou & Danezis 1991). The He and H lines were interpolated in the resulting spectra using a low-order Legendre polynomial fit of the pseudocontinuum around the line. This produced the final estimate of the combined atmospheric and instrumental transmission. We obtained the final J, H, and K band spectra of the science targets by dividing them by this transmission.

We created 1.1–2.5 μm flux-calibrated spectra of the objects using the following procedure. The J, H, and K band ISAAC spectra were convolved with the filter transmission curves. The resulting spectra were integrated. We applied the same procedure to a flux calibrated spectrum of Vega (Mountain et al. 1985; Hayes 1985). We then searched for the normalization factor of the ISAAC spectra that could produce a contrast ratio between the integrated flux of the science target and Vega, which corresponds to the J, H, and K_s-band photometry of the objects taken from 2MASS (Cutri et al. 2003; Allers et al. 2006).

3. Empirical analysis

In this section, we compare the spectral properties of our sample to those of brown dwarfs and companions found in the literature to confirm features indicative of young age and we also assign NIR spectral types for the targets. We select the best of the fit spectrum using χ^2 minimization as well as visual inspection over all of the wavelengths.

For that purpose, we used template spectra of young M- and L-type companions (see the description in Appendix A), late-M and early-L brown dwarfs from star forming regions and young nearby associations (R from ~120 to ~11 500; Gorlova et al. 2003; Slesnick et al. 2004; Allers et al. 2007, 2009, 2010; Lodieu et al. 2008; Rice et al. 2010; Allers & Liu 2013; Bonnefoy et al. 2014a; Manara et al. 2013), young field L dwarfs (R ~ 1500; Kirkpatrick et al. 2006; Allers & Liu 2013; Liu et al. 2013), and MLT field dwarfs (R ~ 2000; McLean et al. 2003; Cushing et al. 2005). We also compared our spectra to low resolution templates (R ~ 120) of the SpeX Prism Spectral Library[1]. Prior to any comparison, the spectrum of Cha J1305 was dereddened by A_V = 3 mag (Allers et al. 2006) using the Fitzpatrick (1999) extinction curve with an interstellar extinction parameter $R(V)$ = 3.1. We assumed A_v = 0 for the remaining targets.

3.1. An age-sequence of M9.5 dwarfs

The spectrum of DENIS-P J124514.1-442907 complements an age sequence of medium-resolution spectra of optically classified M9.5 dwarfs. In Figs. 1–3, we show the J band, H band, and K band, respectively with a resolution of R ~ 1500 in the H and K band and of R ~ 1700 in the J band. This resolution is sufficient to study atomic and molecular lines. The age-sequence is composed of spectra of members of the Taurus (KPNO Tau 4; Briceño et al. 2002), Chameleon I (OTS 44; Oasa et al. 1999; Luhman et al. 2004), and Upper Scorpius (UScoCTIO 108B; Béjar et al. 2008) star forming regions. We also overlay the spectrum of the M10III Mira IO Virginis (Rayner et al. 2009) as an example of an extremely low surface gravity atmospheres. This

[1] http://pono.ucsd.edu/~adam/browndwarfs/spexprism/

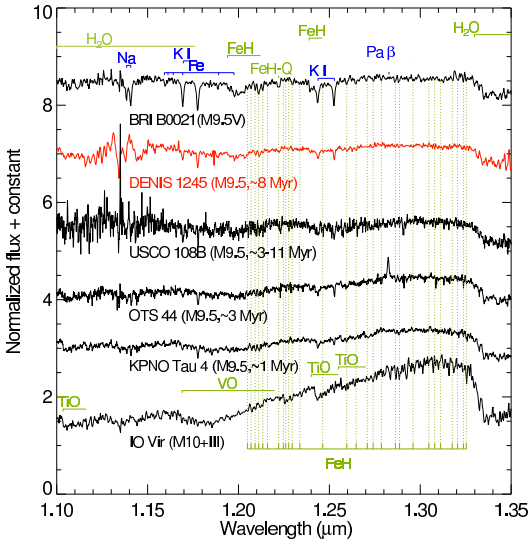

Fig. 1. Spectra of six M9.5 objects with the same optical spectral type, but different ages, i.e., gravity. We can appreciate the evolution of the spectral features with age in the J band. The most remarkable spectral features are the appearance of alkali lines at older ages.

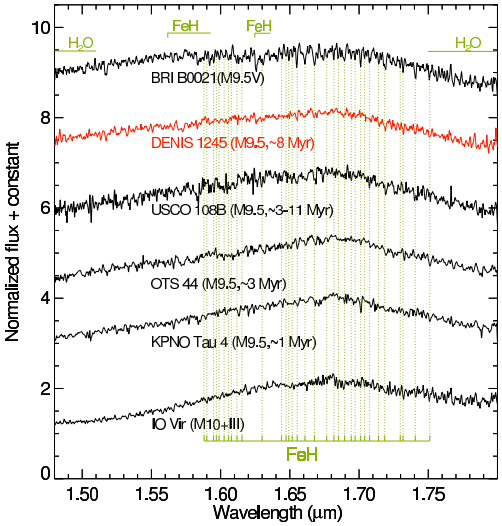

Fig. 2. Same as Fig. 1. Here we appreciate how the H band becomes more triangular when we move to younger BDs.

sequence further highlights age-sensitive and gravity-sensitive features reported in the literature: the increase of the alkali line depths (K I, Na I), an increase in the strength of the FeH absorptions at 1.20 and 1.24 μm, and of the H_2O band (1.7–2.25 μm). The sequence also confirms the decrease of the VO band strength from 1.17 to 1.22 μm and that the J band slope becomes bluer when the age increases, as shown by Kirkpatrick et al. (2006) (see Fig. 1). The other main feature that changes is the progressive appearance of the triangular H band profile when the age decreases, which corresponds to the water absorption profile (Fig. 2). We used these characteristic features to confirm the young age and/or low surface gravity of the Lγ field dwarfs in our sample.

3.2. Young field L-dwarfs?

In this section, we discuss the best-fit spectra for each L-dwarf of our sample. Among the sample of L dwarfs, the Chameleon

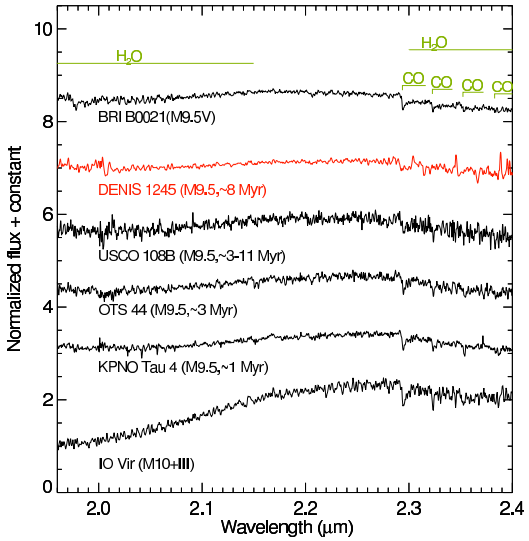

Fig. 3. Same as Figs. 1 and 2 in the *K* band.

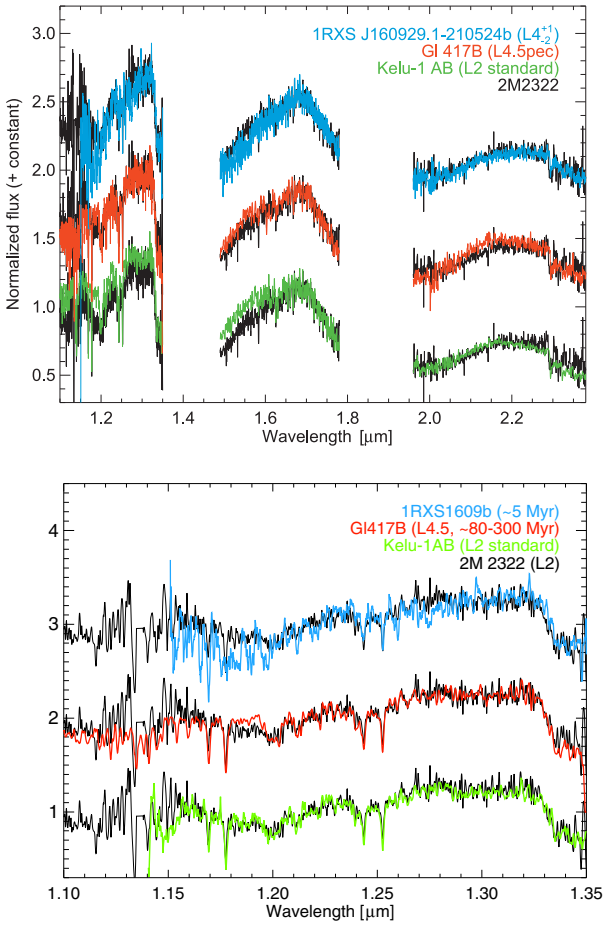

Fig. 4. *Top panel*: comparison of the 1.1–2.38 μm spectrum of the L2γ dwarf 2M2322 to the L2 optical standard (Kelu-1 AB Ruiz et al. 1997; Cushing et al. 2005), of the young L4.5 binary companion GJ 417B (Kirkpatrick et al. 2001; Bonnefoy et al. 2014a), the planetary mass companion 1RXS J160929.1-210524b (Lafrenière et al. 2008, 2010). *Bottom panel*: *J* band in a higher detail.

member Cha J1305-7739 shows clear features indicative of low surface gravity. This is in agreement with the age of the source. The remaining L dwarfs of our sample do not have assigned membership to young moving groups or clusters, and, hence, lack well-determined ages. We therefore tried to identify features in the NIR typical of low surface gravity objects that would confirm the analysis derived by Cruz et al. (2009) in the optical. Plots that show the best matches can be found in the Appendix B, and the most remarkable result is shown in Fig. 4.

The NIR spectrum of the L0γ dwarf EROS J0032 has spectral features midway between the medium-resolution ($R \sim 2000$) NASA Infrared Telescope Facility (IRTF) spectrum (Cushing et al. 2005) of the L1 field dwarf 2MASS J02081833+2542533 and of the M9.5 companion UScoCTIO 108B (Bonnefoy et al. 2014a). The object EROS J0032 has a plateau from 1.59–1.69 μm characteristic of field dwarfs, but a more triangular shape in the *H* band, and weaker FeH, and K I lines in the *J* band. Conversely, it has deeper K I lines (1.169, 1.177, 1.243, 1.253 μm) and FeH bands at 1.2 μm and 1.624 μm than its companion. The 1.1–1.8 μm spectrum of the L0 ± 1 companion to the Upper Scorpius star GSC 06214-00210 (Ireland et al. 2011; Bowler et al. 2011) perfectly reproduces the pseudocontinuum shape of EROS J0032. The companion has nonetheless slightly weaker FeH and K I absorptions. The NIR spectral slope of EROS J0032 is redder than the slope of the L0 field dwarf standard 2MASS J03454316+2540233 (McLean et al. 2003; Kirkpatrick et al. 2010). This can be attributed to reduced CIA of H_2 (Borysow et al. 1997; Kirkpatrick et al. 2006), and, therefore, low surface gravity. The object EROS J0032 also has reduced FeH lines at 1.2 μm and a more triangular *H* band shape than the standard. Nevertheless, the two spectra have comparable K I line depths. The Spectrograph for INtegral Field Observations in the NIR (SINFONI) spectrum of the L0γ benchmark 2MASS J01415823-4633574 (Bonnefoy et al. 2014a) has a more triangular *H* band shape, weaker FeH absorptions, and K I lines than the object. Allers & Liu (2013) and Marocco et al. (2013) also found an indication of low surface gravity in NIR spectra of EROS J0032. The lower-resolution spectrum ($R \sim 100$) of EROS J0032 of Allers & Liu (2013) perfectly matches our ISAAC spectrum. Allers & Liu (2013) assign the same gravity class for this target as for AB Pic b, a ~30 Myr old low-mass L0 (Bonnefoy et al. 2014a) companion. Here, we conclude that EROS J0032 only shows *moderate* signs of low surface gravity.

The object EROS J0032 and the second L0γ dwarf of our sample 2M2213 have comparable NIR spectral slopes. Nevertheless, we find that 2M2213 has a *H* band shape, K I and FeH line depths midway between those of EROS J0032 and UScoCTIO 108B. Therefore, this comparison suggests that 2M2213 has a lower surface gravity and is younger age than EROS J0032, but is older than the assumed age of Upper Scorpius (~5–11 Myr; Preibisch & Zinnecker 1999; Slesnick et al. 2008; Pecaut et al. 2012). Marocco et al. (2013) also obtained a medium-resolution NIR spectrum of this object, and reach similar conclusions. They classify it as a L2pec based on the good match with the NIR spectrum of a field L2 standard. Nevertheless, such a comparison can not be done for young objects (Luhman et al. 2004), as it can lead to later spectral type estimates. To conclude, we find that our spectrum perfectly matches the low-resolution ($R \sim 100$) spectrum of 2M2213 obtained by Allers & Liu (2013).

In Fig. 4 we show that the spectrum of the L2γ dwarf 2M2322 is reproduced by the spectrum (Bonnefoy et al. 2014a) of the moderately old L4.5+L4.5 binary companion GJ417 B (age from 80 to 890 Myr, Kirkpatrick et al. 2001; Allers et al. 2010). But the object exhibits weaker FeH absorption,

and K I lines than its companion. The pseudocontinuum shape of 2M2322 from 1.95 to 2.5 μm, and from 1.45 to 1.6 μm is midway between the one of GJ 417 B and of the 5–11 Myr old L4 planetary mass companion 1RXS J160929.1-210524b (Lafrenière et al. 2008, 2010). All three objects have similar NIR spectral slopes. The object 2M2322 also has a slightly redder spectral slope, more triangular H band, and bumpy pseudocontinuum in the K band than the L2 field dwarf standard Kelu-1 AB (Cushing et al. 2005; Kirkpatrick et al. 2010). All of these comparisons provide evidence that this object has a low surface gravity. As a by-product, the companion suggests that 1RXS J160929.1-210524b has a spectral type L2.

The 1.1–2.5 μm pseudo-continuum of 2M2126 is well reproduced by the spectrum of the young (~20–300 Myr Zapatero Osorio et al. 2010) L3γ companion G 196-3B (Rebolo et al. 1998) gathered by Allers & Liu (2013). The depth of alkali-lines and of the FeH absorption at 1.2 μm are similar for the two objects. Nevertheless, the water-band absorptions from 1.33–1.35 μm and 1.45–1.6 μm are deeper in the companion spectrum. The spectral slope from 1.2–1.33 μm is also redder in the spectrum of G 196-3B. We also find a good match with the spectrum of the brown dwarf companion CD-35 2722B (Wahhaj et al. 2011), classified as L3 by Allers & Liu (2013). The object CD-35 2722 B forms a coeval system with CD-35 2722 A, a member of the 75–150 Myr old AB Doradus association. We then conclude that 2M2126 is a young object, with indications of reduced surface gravity, and features in the NIR consistent with its optical class L3γ determined by Cruz et al. (2009).

The second L3γ dwarf of the sample, 2M2208, has an identical spectrum to 2M2126. Both objects show comparable K I and FeH line depths in the J band, and a similar gravity-sensitive slope from 1.45 to 2.29 μm. Nevertheless, this object has a bluer 1.1–2.5 μm slope than 2M2126 (and therefore G196-3B). The blue slope likely arises from an improper scaling of the J, H, K band spectra due to uncertainty in the photometry. Indeed, the 1.1–1.35 μm portion of the spectrum has a slightly higher flux than the low-resolution ($R \approx 100$) spectrum of the source obtained by Allers & Liu (2013), but a similar pseudocontinuum otherwise. The slope is better reproduced by the spectrum of GJ417 B (Kirkpatrick et al. 2001; Bonnefoy et al. 2014a) and by an IRTF spectrum of the L3 field dwarf 2MASS J15065441+1321060 (Reid et al. 2000; Cushing et al. 2005). But the KI and FeH lines are weaker in the spectrum of 2M2208 than in the spectra of these two objects. Therefore, the analysis confirms that 2M2208 shows signature characteristics of young L3–L5 objects, and a spectral type similar to that of 2M2126.

3.3. Indices and equivalent widths

To further assess the age, surface gravity, and spectral classes of our targets, we computed spectral indices and equivalent widths that quantify the evolution of the main absorption features.

We first used spectral indices measuring the strength of the main water bands. These indices were selected independently by Bonnefoy et al. (2014a) and/or Allers & Liu (2013) from Allers et al. (2007) – H_2O, Slesnick et al. (2004) – H_2O-1 and H_2O-2, and McLean et al. (2003) – H_2OD. They are known to show a clear trend with the spectral type, and to be only weakly sensitive to the age or to the gravity class (γ, β). We computed them on the compilation of NIR spectra of young M3–M9.5 dwarf members of star forming regions (1–11 Myr) and young nearby associations (age <50 Myr) classified in the optical. We also derived them for young Lγ, Lβ dwarfs, and companion spectra provided by Allers & Liu (2013) and Bonnefoy et al. (2014a), and

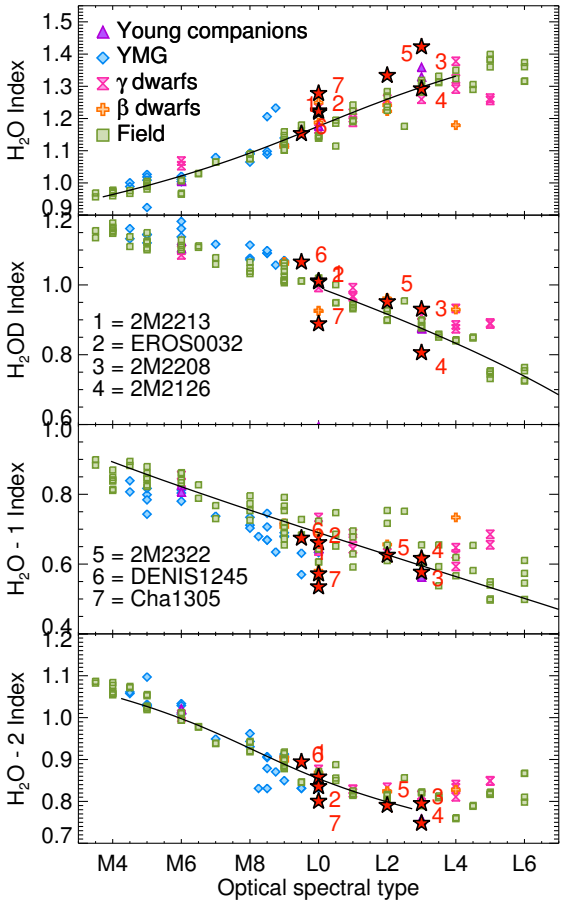

Fig. 5. Spectral indices used for the spectral type estimation of the NIR spectral type. Our targets are represented by red stars and are numbered from 1 to 6: 1 = 2M2213, 2 = EROS J0032, 3 = 2M2208, 4 = 2M2126, 5 = 2M2322, 6 = DENIS 1245 and 7 = Cha1305. The black lines represent the three-degree polynomial fit to the field brown dwarfs. We report the index values for objects classified in the optical that are members of young clusters, star forming regions, or nearby associations (YMG), and for dwarfs with low (γ) and intermediate (β) gravity classes (Kirkpatrick 2005).

for field dwarfs obtained by McLean et al. (2003) and Cushing et al. (2005). We degrade the resolution of all the spectra to $R \sim 100$, which is our lowest resolution. Results are shown in Fig. 5. We reajusted a third-order polynomial function on these trends (Table 2), as in Allers & Liu (2013), and use them to derive spectral type estimates (Table 3). We calculated the errors in the spectral type as the root mean square (rms). We estimated the final NIR spectral types, obtaining the mean of the different estimates from the indices weighted by the associated error, and their errors, as the standard deviation. These estimates are all consistent with the optical spectral types. They are also consistent with the matches found in Sect. 3.2.

The equivalent widths of the gravity-sensitive K I lines at 1.169 μm, 1.177 μm, 1.243 μm, and 1.253 μm of our objects are reported in Table 4. They were computed following the method developed by Sembach & Savage (1992). We used the same reference wavelengths for the fit of the pseudocontinuum and for the line as Allers & Liu (2013). In Fig. 6, we show the equivalent widths of these lines as for our targets and reference objects. The trends are similar to those found by Bonnefoy et al. (2014a) and Allers & Liu (2013). For all four cases, EROS J0032 has an equivalent widths close to those of field L0 dwarf analogues. The remaining field Lγ dwarfs have

Table 2. Coefficient of the polynomial fit derived from index values computed on field dwarf spectra and shown in Fig. 5.

Index definition	References	SpT	Coefficients of polynomial fits				RMS Sp. type
			a	*b*	*c*	*d*	
$H_2O = \frac{\langle F\_\lambda=[1.550,1.560]\rangle}{\langle F\_\lambda=[1.492,1.502]\rangle}$	Allers et al. (2007)	M4–L4	–199.72	487.93	–394.58	111.66	1.0
$H_2OD = \frac{\langle F\_\lambda=[1.951,1.977]\rangle}{\langle F\_\lambda=[2.062,2.088]\rangle}$	McLean et al. (2003)	L0–L6	20.16	10.28	–24.13	3.48	1.0
$H_2O\text{-}1 = \frac{\langle F\_\lambda=[1.335,1.345]\rangle}{\langle F\_\lambda=[1.295,1.305]\rangle}$	Slesnick et al. (2004)	M4–L6	29.42	–17.94	–24.98	14.73	0.5
$H_2O\text{-}2 = \frac{\langle F\_\lambda=[2.035,2.045]\rangle}{\langle F\_\lambda=[2.145,2.155]\rangle}$	Slesnick et al. (2004)	M4–L3	306.25	–917.19	965.74	–348.88	1.0

Table 3. Estimation of the NIR spectral types based on spectral indices.

Name	Opt SpT	Reference	Empirical SpT	Index SpT				NIR SpT
				H_2O	H_2OD	H_2O-1	H_2O-2	
DE J1245	M9.5	1	M9	M9.5 ± 1.0	M8.0 ± 1.0	L0.5 ± 0.5	M9.0 ± 1.0	M9.5 ± 1.0
EROS J0032	L0γ	2,6	L1	L1.0 ± 1.0	L0.0 ± 1.0	L1.0 ± 0.5	L0.5 ± 1.0	L0.5 ± 0.5
2M J2213	L0γ	8	L0	L1.0 ± 1.0	M9.5 ± 1.0	L3.5 ± 0.5	L0.0 ± 1.0	L2.0 ± 1.5
Cha J1305	L0	3,7	L1	L2.5 ± 1.0	L2.5 ± 1.0	L5.0 ± 0.5	L2.0 ± 1.0	L3.5 ± 1.5
2M J2322	L2γ	4, 8	L2	L4.0 ± 1.0	L1.0 ± 1.0	L2.0 ± 0.5	L2.5 ± 1.0	L2.0 ± 1.0
2M J2126	L3γ	4, 8	L3	L3.0 ± 1.0	L5.5 ± 1.0	L2.0 ± 0.5	L4.5 ± 1.0	L3.0 ± 1.5
2M J2208	L3γ	5, 8	L1	L7.0 ± 1.0	L2.0 ± 1.0	L3.5 ± 0.5	L2.0 ± 1.0	L3.0 ± 2.0

References. [1] Looper et al. (2007); [2] Reid et al. (2008); [3] Allers et al. (2006); [4] Reid et al. (2008); [5] Allen et al. (2007); [6] Allers & Liu (2007); [7] Alcalá et al. (2008); [8] Cruz et al. (2009).

Table 4. Age-sensitive indices and equivalent widths.

Object	FeH_J[a]	KI_J[a]	H-cont[a]	EW – K I 1.169 μm (Å)	EW – K I 1.177 μm (Å)	EW – K I 1.243 μm (Å)	EW – K I 1.253 μm (Å)
DE J1245	1.091 ± 0.005	1.058 ± 0.002	0.992 ± 0.001	2.20 ± 0.57	2.57 ± 0.76	2.05 ± 0.13	1.02 ± 0.12
EROS J0032	1.200 ± 0.003	1.096 ± 0.005	0.925 ± 0.001	5.92 ± 0.31	9.30 ± 0.41	5.97 ± 0.17	4.46 ± 0.16
2M J2213	1.134 ± 0.004	1.034 ± 0.004	0.958 ± 0.002	7.45 ± 0.92	12.45 ± 1.31	1.31 ± 0.28	1.94 ± 0.25
2M J2322	1.144 ± 0.009	1.112 ± 0.003	0.935 ± 0.001	3.86 ± 0.56	7.78 ± 0.74	5.78 ± 0.21	4.51 ± 0.19
2M J2126	1.183 ± 0.010	1.061 ± 0.003	0.949 ± 0.001	4.98 ± 0.34	6.55 ± 0.46	4.43 ± 0.22	4.52 ± 0.20
2M J2208	1.118 ± 0.010	1.063 ± 0.003	0.930 ± 0.001	7.69 ± 0.41	8.39 ± 0.55	7.43 ± 0.39	3.86 ± 0.36

Notes. [(a)] Computed using the code developed by Allers & Liu (2013).

lower equivalent widths in some, but not all of the diagrams. This confirms the conclusions derived in Sect. 3.2. The object DENISJ1245 has equivalent widths comparable as late-M dwarf members of the ∼8 Myr old TW Hydrae and Upper Scorpius. This is consistent with the membership of this object to the TW Hydrae association (see Looper et al. 2007, and Sect. 5.2.1). We calculate the KI_J index for medium-resolution spectra degraded at $R \sim 700$. We find similar results and trends (Fig. 7) in the KI_J index defined by Allers & Liu (2013), and measure the depth of the K I doublet at 1.243–1.253 μm. The spectrum of Cha J1305 was too noisy to derive equivalent widths and KI_J index values.

We also computed the FeH_J and H-cont indices defined by Allers & Liu (2013). These indices measure the strength of the gravity sensitive FeH feature at 1.2 μm and the shape of the H band continuum, respectively. We calculate the FeH_J index using medium-resolution spectra degraded at $R \sim 700$. Nonetheless, we use all the spectra smoothed to $R \sim 100$ to calculate the H-cont index, as the H band is broad enough not to be significantly affected by the spectral resolution. The index values are reported for the targets in Table 4 and compared to other objects in Fig. 7. All the objects, except EROS J0032 have index compatible with the trends of objects from young moving groups and γ and β dwarfs. This further indicates that EROS J0032 is the object with the highest surface gravity and/or the oldest age of the sample.

4. Spectral synthesis

In the following sections, we compare the dereddened NIR spectra of our objects to predictions from BT-Settl atmospheric models (Allard et al. 2003a, 2007, 2011). The models have already been tested on NIR spectra of young M5.5–L0 objects by Bonnefoy et al. (2014a). We compare the new ISAAC spectra to derive the atmospheric parameters ($T_{\rm eff}$, $\log g$) of the objects and to reveal non-reproducibilities of the models for later spectral types. Flux in synthetic spectra are provided per cm^2 of the stellar surface. They therefore need to the scaled back, using the distance modulus, to absolute flux. The models are described in Allard et al. (2011, 2012a,b). We summarize their most relevant characteristics below.

The BT-Settl models account for the formation and gravitational settling of dust grains for $T_{\rm eff}$ below ≈2700 K in the photosphere of the objects, following the approach described in Rossow (1978). The timescales of the main processes (mixing, sedimentation, condensation, coalescence, and coagulation) are compared to determine the density distribution of grains and the

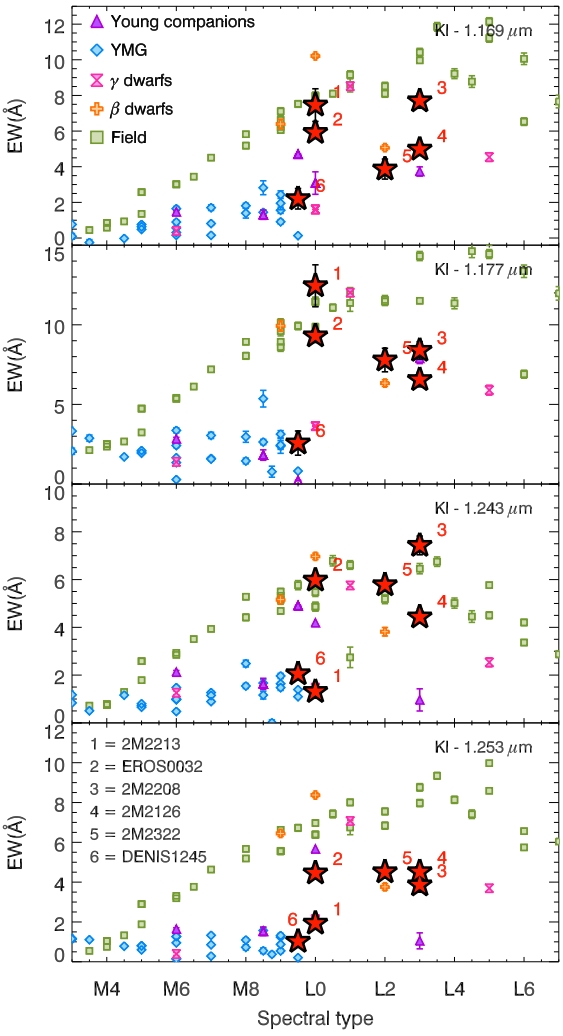

Fig. 6. Equivalent widths for the K I lines at 1.169 μm, 1.177 μm, 1.243 μm, and 1.253 μm for our targets (red stars) and reference objects.

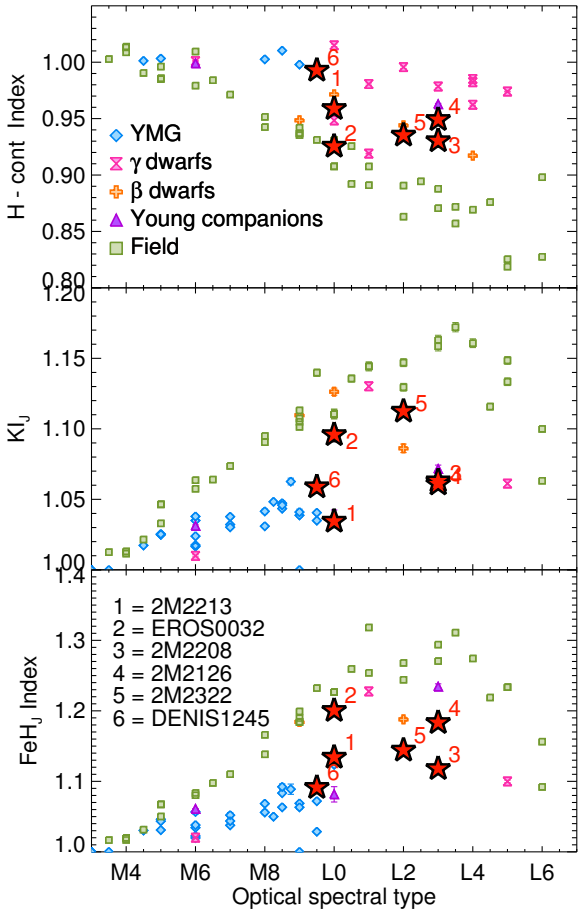

Fig. 7. FeH, KI$_J$, and H band age-sensitive indices.

average grain size from the innermost to the outermost layers of the cloud. The model accounts for one hundred and eighty types of condensates via their interaction with the gas phase chemistry, depleting the gas from their vapor phase counterparts. Fifty-five of these grain species are included in the radiative transfer to the extent to which they have not settled from the cloud layer.

The cloud model is implemented in the PHOENIX multipurpose atmosphere code version 15.5 (Allard et al. 2001), which is used to compute the model atmospheres and to generate synthetic spectra. Convective energy transport and velocities are calculated using mixing length theory with a mixing length of 2.0 pressure scale heights, and overshoot is treated as an exponential velocity field with a scale height based on the RHD simulations of Ludwig et al. (2002, 2006) and Freytag et al. (2010, 2012); an additional advective mixing term due to gravity waves is included as described in Freytag et al. (2010). All relevant molecular absorbers are treated with line-by-line opacities in direct opacity sampling as in Allard et al. (2003b); regarding this, the molecular line lists have been updated as follows: water-vapor (BT2, Barber et al. 2006), CIA of H_2 (Borysow 2002), and FeH (Plez 1998; Weck et al. 2003; Dulick et al. 2003). Nonequilibrium chemistry for CO, CH_4, CO_2, N_2, and NH_3 is treated with height-dependent diffusion also based on the RHD simulation results of Freytag et al. (2010).

We used the 2010 and 2013 prereleases of these models[2]. The comparative analysis of the results provided by these two versions enables us to judge the pertinence of new physics incorporated. With this approach, we also avoid relying only on the most recent version of the models, which remain to be tested, contrary to the BT-Settl 2010 models (e.g. Bonnefoy et al. 2014a). In the 2013 pre-release of the BT-Settl models (hereafter BT-Settl 2013, Allard et al. 2011), the cloud model was improved with a dynamical determination of the supersaturation, the implementation of a grain size-dependent forward scattering, and by accounting for grain nucleation based on cosmic rays studies (Tanaka 2005). The BT-Settl 2010 models rely on the reference solar abundances of Asplund et al. (2009). Conversely, the BT-Settl 2013 models are based on the CIFIST photospheric solar abundances of Caffau et al. (2011). Therefore, the 2013 solarmetallicity models have atmospheres slightly enriched with C, O compared to the 2010 models, e.g., in elements involved in the formation of the main molecular absorbers in the NIR (CO, H_2O) and of dust grains

[2] The 2013 prerelease of the models corresponds to the final and stable version of the 2012 model grid (called BT-Settl 2012; used in Bonnefoy et al. 2013, 2014a,b) where some synthetic spectra were recomputed following the discovery of errors in the model code. Upgrades in the 2012 grid were released progressively on the *Star, Brown Dwarf & Planet Simulator* web server (http://phoenix.ens-lyon.fr/Grids/BT-Settl/CIFIST2011/RESTARTS/) until September 2013. Therefore, we decided to call the most recent version of the models used in this study *BT-Settl 2013*, even if a new version of the BT-Settl models may be released on the web server by the end of 2013.

Table 5. Atmospheric parameters corresponding to the best fit spectra or synthetic fluxes for our seven targets.

Model	Band	DENIS J1245	EROS J0032	2M2213	Cha 1305	2M 2322	2M 2126	2M 2208
BT-Settl 2010	*J*	2300/3.5/0.0	2100/3.5/0.0	1700/4.5/0.0	1700/3.5/0.0	2000/3.5/0.0	2000/3.5/0.0	1700/4.0/0.0
BT-Settl 2010	*H*	2300/3.5/0.0	2100/3.5/0.0	1700/4.5/0.0	2100/3.5/0.0	2200/3.5/0.0	1600/3.5/0.0	1800/3.5/0.0
BT-Settl 2010	*K*	2400/3.5/0.0	2000/4.5/0.0	1700/4.5/0.0	1700/3.5/0.0	2000/4.0/0.0	2100/4.0/0.0	1700/4.0/0.0
BT-Settl 2010	*JHK*	2400/3.5/0.0	2000/4.5/0.0	1700/3.5/0.0	1700/3.5/0.0	1700/3.5/0.0	1600/3.5/0.0	1800/3.5/0.0
BT-Settl 2010	*SED*	2200/3.5/0.0	2000/4.5/0.0	2000/3.0/0.0	...	1800/3.5/0.5	1800/3.5/0.0	1800/4.0/0.0
BT-Settl 2013	*J*	2400/3.0/0.0	1700/5.0/0.5	1800/4.5/0.5	1800/4.5/0.5	1800/4.5/0.5	1800/4.5/0.5	1900/4.0/0.5
BT-Settl 2013	*H*	2400/3.0/0.0	1800/4.5/0.5	1800/4.5/0.5	1800/4.5/0.5	1800/4.5/0.5	1800/4.5/0.5	1800/4.5/0.5
BT-Settl 2013	*K*	2400/3.0/0.0	1800/4.5/0.5	1800/4.5/0.5	1800/4.5/0.5	1800/4.5/0.5	1800/4.0/0.0	1800/4.0/0.0
BT-Settl 2013	*JHK*	2400/3.0/0.0	1800/4.5/0.5	1800/4.5/0.5	1800/4.5/0.5	1800/4.5/0.5	1800/4.0/0.0	1800/4.5/0.0
BT-Settl 2013	*SED*	2100/3.0/0.0	1900/4.0/0.5	1800/4.5/0.0	...	1800/3.5/0.5	1800/3.5/0.0	1800/4.0/0.0

Notes. We give $T_{\rm eff}$/ log g/[M/H].

(e.g., Forsterite – Mg_2SiO_4, Ensaltite – $MgSiO_3$), which either contribute to the atmospheric opacity or deplete the gas phase from elements.

We selected subgrids of synthetic spectra with 1000 K $\leq T_{\rm eff} \leq$ 3000 K, 3.0 $\leq \log g \leq$ 5.5 ($\geq$3.5 below 2000 K), and [M/H] = 0. An alternative subgrid of the BT-Settl 2013 models (1000 K $\leq T_{\rm eff} \leq$ 3000 K, 3.5 $\leq \log g \leq$ 5.5) with M/H = +0.5 dex was also used to explore the effect of the metallicity on the determination of log g and $T_{\rm eff}$. The spacing of the model grid is 100 K and 0.5 dex in log g.

4.1. Near-infrared spectra

The BT-Settl 2010 and the 2013 synthetic spectra were smoothed to the resolution of ISAAC. The models were then reinterpolated on the ISAAC wavelength grid. Spectra were normalized in the following wavelength intervals 1.1–1.35 μm (*J*), 1.46–1.80 μm (*H*), 2.02–2.42 μm (*K*), and 1.1–2.42 μm (*JHK*), and compared in these intervals using least-squares. Results from the fit were always checked visually. This often revealed inapropriate fitting solutions induced by the remaining uncertainties in the models. Fits with the BT-Settl 2010 model spectra were, in particular, affected by a numerical noise introduced by the limited original wavelength sampling of the models (Bonnefoy et al. 2014a). The fits with the BT-Settl 2013 models were more affected by the nonsimultaneous fit of the water bands longward 1.33 μm and by the improper modeling of the *H* band shape. Atmospheric parameters corresponding to the best fit models are reported in Table 5. The parameters $T_{\rm eff}$, log g, and M/H have minimum uncertainties of 100 K, 0.5 dex, and 0.5 dex respectively. These errors correspond to the sampling of the atmospheric parameters of the model grids. We show the best fit synthetic spectra in Figs. 8 to 11.

BT-Settl models reproduce the shape of the pseudocontinuum and of the prominent narrow atomic (K I, Na I) and molecular (CO) lines of the objects when each band is fitted independently from each other. We recover the non-reproducibility from 1.6 to 1.7 μm and from 1.195–1.205 μm quoted in Bonnefoy et al. (2014a) and, it is at least partially, due to missing FeH opacities. The ability to reproduce the data is worse in the case of EROS J0032. The spectrum of this object has features more typical of mature field dwarfs (Sect. 3). This miss-match is consistent with the conclusions of Bonnefoy et al. (2014a), who find a similar departure of the models at these wavelengths in field L-dwarf spectra.

The surface gravity of Cha1305 and DENIS J1245 found with BT-Settl 2010 falls in the range expected from evolutionary models for 1–10 Myr objects. It also corresponds, within error bars, to the one determined for late-M/early-L targets from Chameleon and TW Hydrae by Bonnefoy et al. (2014a) based on the same analysis tools and models. The BT-Settl 2013 models fit a higher surface gravity and metallicity to the spectrum of Cha1305. The two parameters are known to have counteracting effects on the atmospheric pressure at a given optical depth (see Mohanty et al. 2007) and dust content in the atmosphere. They can then induce opposite variations of the main spectroscopic features (Looper et al. 2008). Therefore, the higher surface gravity found for Cha1305 is likely caused by the degenerate effect of metallicity. We find an alternative solution with a lower surface gravity for this object at solarmetallicity (see Fig. 11), which provides a good fit of the 1.1–2.5 μm spectrum, but fails to reproduce the shape of the pseudocontinuum in the *H* band.

The fit of the *J*, *H*, and *K* band spectra do not reveal a clear correlation between the spectral type and the temperature when the 2010 release of the models is used. The best fit temperatures can vary by up to 500 K from band to band. The 1.1–2.5 μm spectra are also fitted by models at lower temperatures, with differences of 500 K. The spread in effective temperature is reduced to 200 K with the 2013 models. Nevertheless, the solutions found fitting the 1.1–2.5 μm spectrum of the objects provides a reasonable fit in the individual bands with both models.

The reduced scatter in effective temperatures found with the 2013 release of the models also reflects the overall better quality of the fit provided by these models. The BT-Settl 2010 models reproduce better the spectra than the 2013 models when solarmetallicity models are considered. These behaviors are closely related to the dust that is allowed to form and is sustained in the atmospheres of both models. We discuss these differences in Sect. 5.1.

We decided to further test the models by comparing their predictions to the 1–5 μm spectral energy distributions of the objects.

4.2. Spectral energy distributions

We built the spectral energy distributions (SED) of the sources using published photometry from the 2MASS (*J*, *H*, *K* bands; $\lambda_{\rm ref}$ = 1.235, 1.662, and 2.159 μm; Cutri et al. 2003) and WISE (W1, $\lambda_{\rm ref}$ = 3.4 μm; W2, $\lambda_{\rm ref}$ = 4.6 μm; Cutri & et al. 2012) sky surveys. The sources also have W3 ($\lambda_{\rm ref}$ = 12 μm) and W4 ($\lambda_{\rm ref}$ = 22 μm) WISE photometry. Nevertheless, we refrained from accounting for this photometry in the fit since the sources were not detected at a good S/N (>8) in the WISE images. We excluded Cha 1305 from this analysis since the SED of this source has a strong excess (Allers et al. 2006). The optical photometry, avaliable for some objects, is not included in the fit

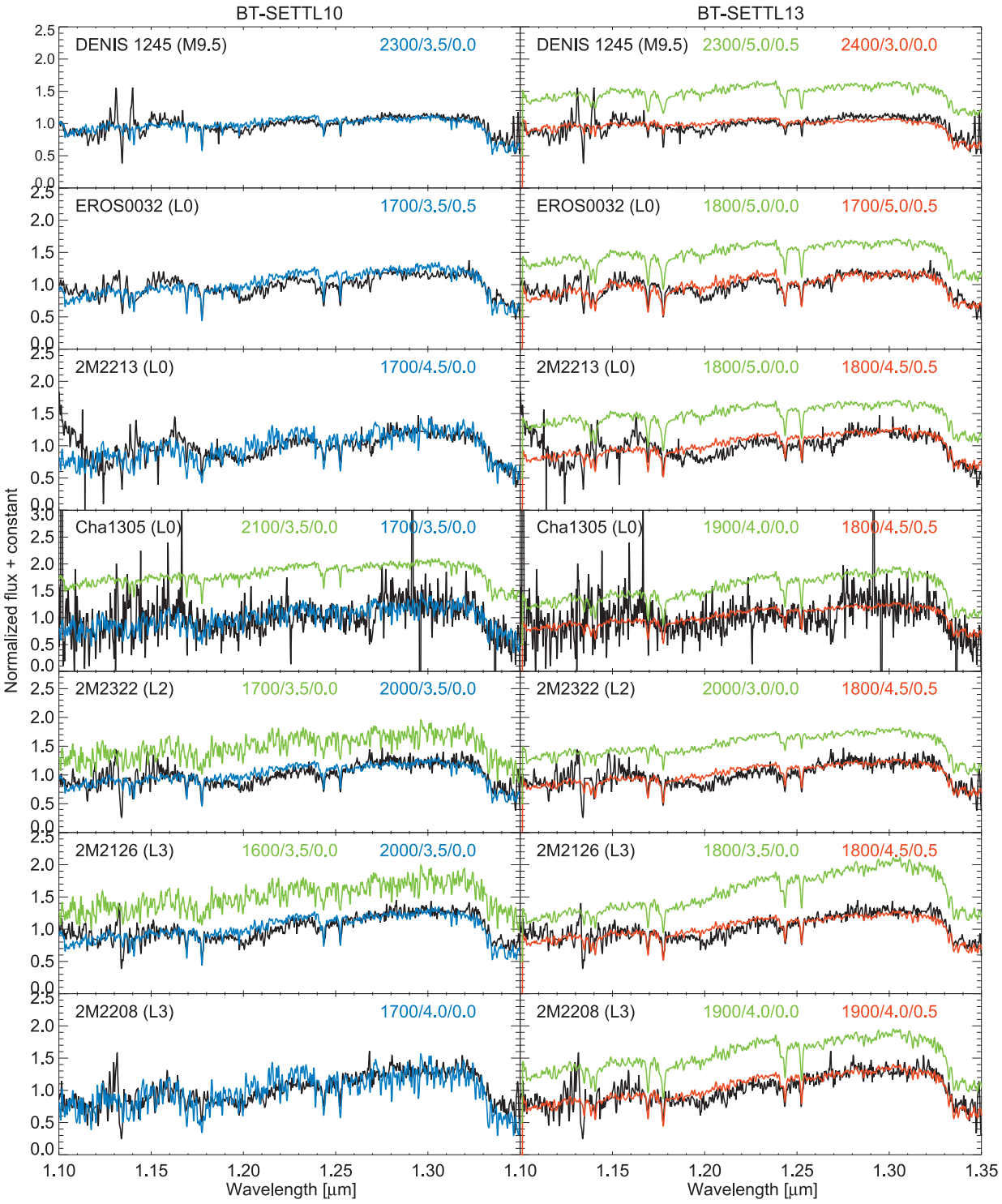

Fig. 8. Visual comparison of the best fit BT-Settl 2010 (*left column*, blue) and BT-Settl 2013 (*right column*, red) synthetic spectra to the six new ISAAC spectra of young M9.5–L3 dwarfs in the *J* band (1.1–1.35 μm). All spectra have been normalized over the wavelength interval. Alternative solutions are shown in light green and are shifted by +0.3 to +0.5 flux normalized units for clarity.

because the models are known to be inaccurate at these wavelengths (see Bonnefoy et al. 2014a).

The infrared photometry was converted to fluxes using tabulated zero points (Cohen et al. 2003; Jarrett et al. 2011).

We generated synthetic fluxes from the BT-Settl 2010 and 2013 model grids in the passbands corresponding to the available photometry of the sources. The synthetic fluxes (F_λ) are provided per square centimeters of the stellar surface. The synthetic SEDs were then normalized to the object apparent fluxes by scaling a dillution factor that minimized the χ^2 of the fit. This dillution factor corresponds to R^2/d^2, in which R and d are the radius and distance of the source, respectively.

The best-fit atmospheric parameters corresponded to the minimimum χ^2 of the fit found for all possible combinations of atmospheric parameters in the grid of models. These parameters are reported in Table 5. The corresponding spectra are shown

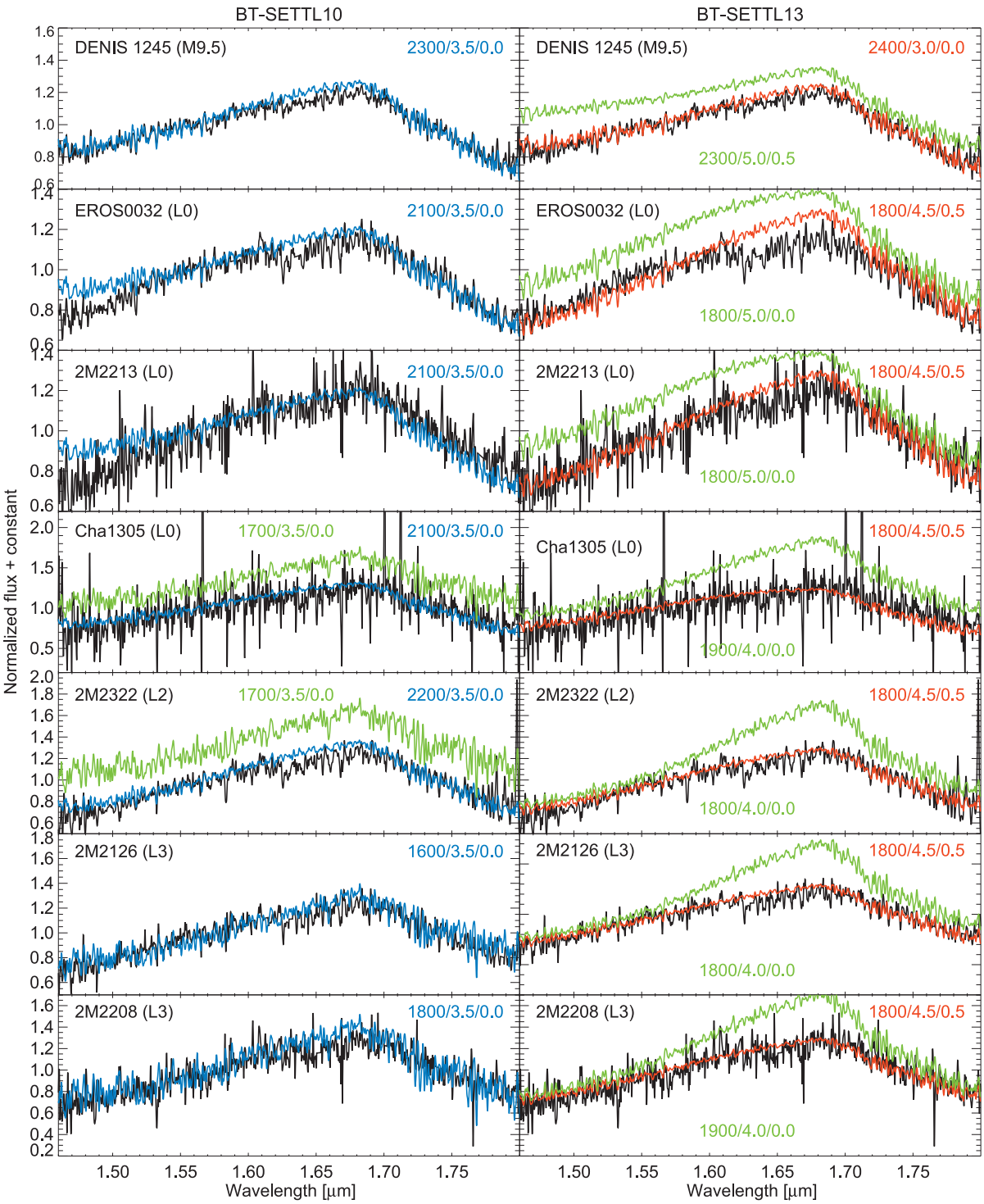

Fig. 9. Same as Fig. 8, but in the H band (1.46–1.8 μm).

in Fig. 12. χ^2 maps indicate that for most of the objects the fit is sensitive to $T_{\rm eff}$ only. We estimate errors of $^{+300}_{-100}$ K for DENIS 1245, and ±100 K for the remaining targets with the BT-Settl 2013 models. We also find errors of $^{+100}_{-500}$ K for 2M2213 and 2M2322, and ±200 K otherwise for the BT-Settl 2013 models. These errors are based on 5σ contours in the χ^2 maps. Both models yield similar effective temperatures (±200 K). This is not surprising since differences between the models are expected to vanish at the spectral resolution corresponding to the broad-band filters considered here. This also indicates that the errors are conservative.

Semiempirical radii R can be derived for the objects with known distances d from the normalization factor R^2/d^2 used to scale the model SED to the flux of the object. This is the case for EROS J0032 and DENIS 1245 (see Sect. 5.2). We therefore derive $R = 0.9 \pm 0.2\ R_{\rm Jup}$ for EROS J0032 and $R = 2.4 \pm 0.6\ R_{\rm Jup}$ for DENIS 1245 from the two sets of models. We compare these values to predictions from evolutionary models in Sect. 5.2.

The SED fit confirms the effective temperatures found from the NIR spectra. Two objects (2M2322, and 2M2126) have best-fit temperatures which disagree with those found from the fit of the BT-Settl 2010 models to the 1.1–2.5 μm spectra. We selected

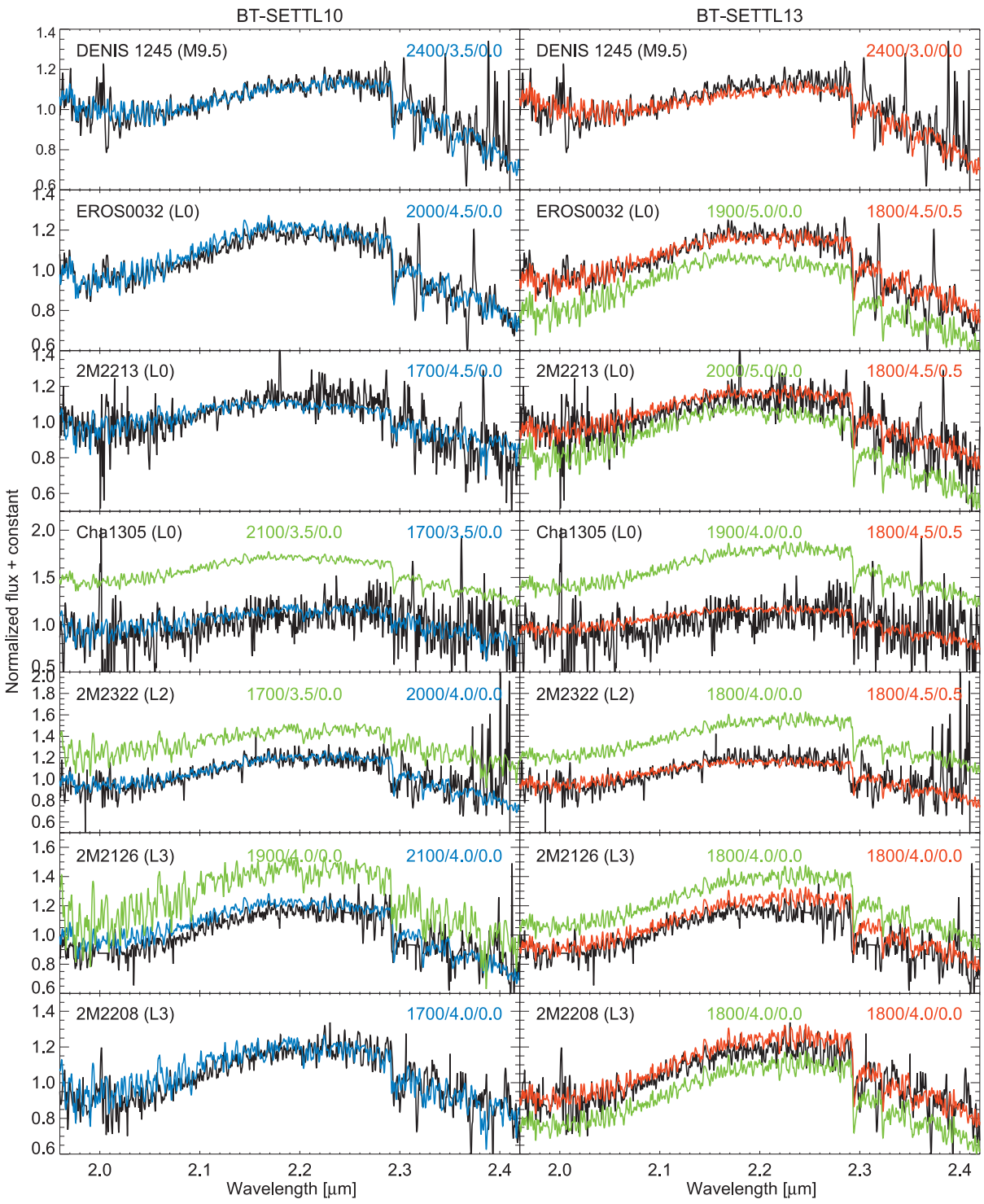

Fig. 10. Same as Fig. 8, but in the *K* band (1.96–2.42 μm).

a subgrid of synthetic spectra corresponding to the set of atmospheric parameters producing the best fit of the SED within a 5σ confidence level. We identified the spectrum from this sub-grid producing the best fit of the 1.1–2.5 μm spectra of the targets, and displayed them in Fig. 13. The best fits are found for low surface gravities, therefore further confirming results from the empirical analysis. Nevertheless, the comparison demonstrates that the models do not successfully reproduce the global spectral slope at these wavelengths as well as the pseudocontinuum in the *H* band. We reach similar conclusions for DENIS 1245, whose fit also indicates a mismatch of the overall spectral slope by the models if reduced (3σ) errors are considered on the temperature derived from the SED. We discuss possible explanations for the non-reproducibility of the models in the following section.

5. Discussion

5.1. Behavior of atmospheric models

The atmospheric models yield atmospheric parameters that are mostly consistent with our empirical analysis. All of the

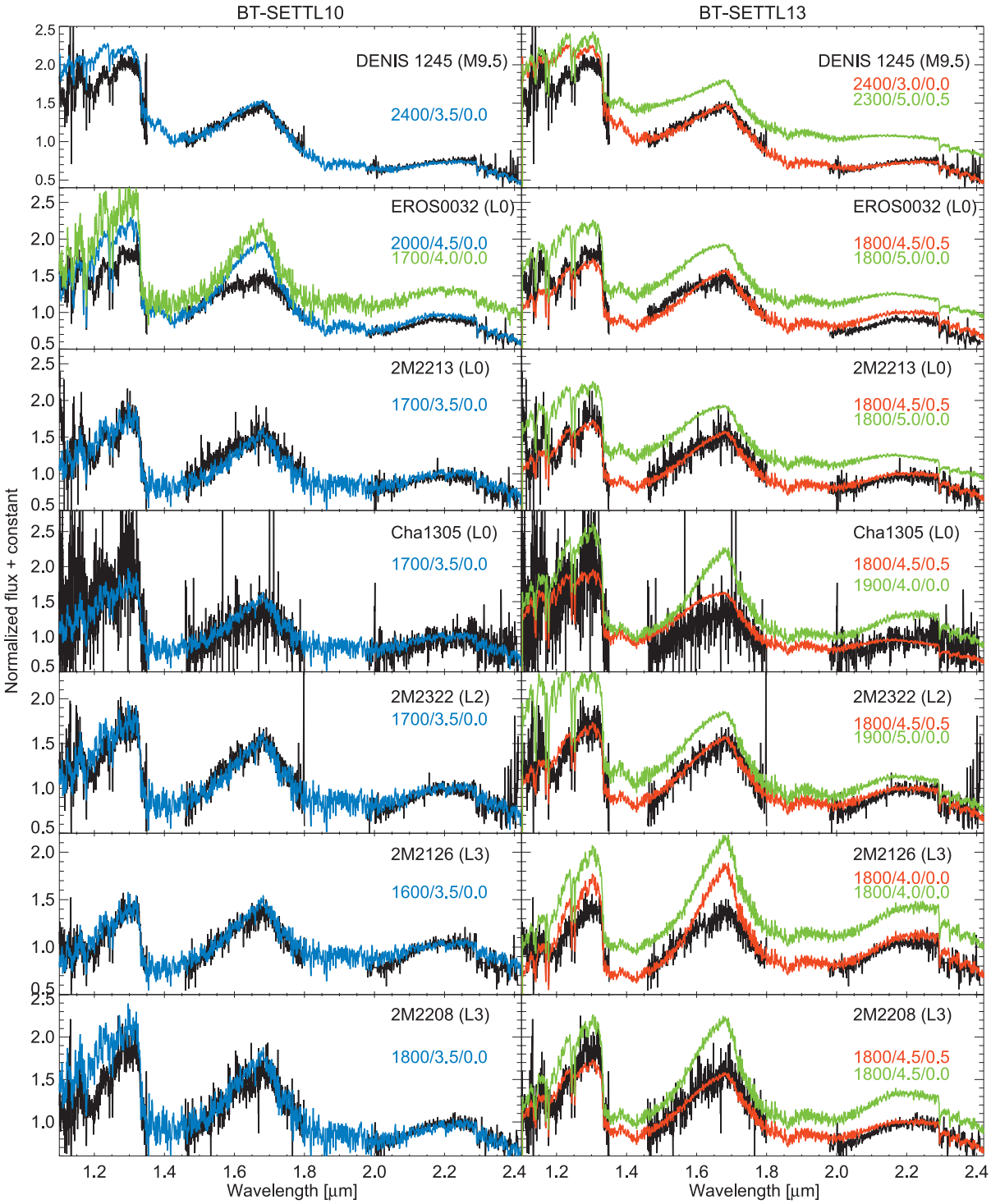

Fig. 11. Same as Fig. 8, but for the whole NIR spectrum (1.1–2.42 μm).

Lγ objects have surface gravities expected for young objects. The BT-Settl 2013 models converge toward an overall higher surface gravity for EROS J0032.

Surprisingly, all spectra but that of DENIS 1245 are well reproduced by a single BT-Settl 2013 synthetic spectrum with $T_{\rm eff}$ = 1800 K, $\log g$ = 4.5, and M/H = +0.5. Models at higher metallicity used in this analysis had not been extensively tested and suffer from increased numerical instability due to the dust content in these atmospheres that is several times greater. Nonconvergent models can indeed have an anomalous dust content, which can sometimes produce spectra that match the observations well. We found nonetheless that a neighboring spectra with $T_{\rm eff}$ = 1700 K and $\log g$ = 4.5 is affected by this problem. Therefore, it is possible that our temperature estimate could be biased by 100 K given our inability to check if a convergent model at these $T_{\rm eff}$ can provide a better fit. We also verified that the features of the model spectrum at $T_{\rm eff}$ = 1800 K are coherent with those found in model spectra for other neighboring $T_{\rm eff}$ and $\log g$.

The NIR spectral slopes, and therefore results from the fits of the ISAAC spectra, are mostly tied to the dust content in the atmosphere. Solutions at high metallicity can then be interpreted

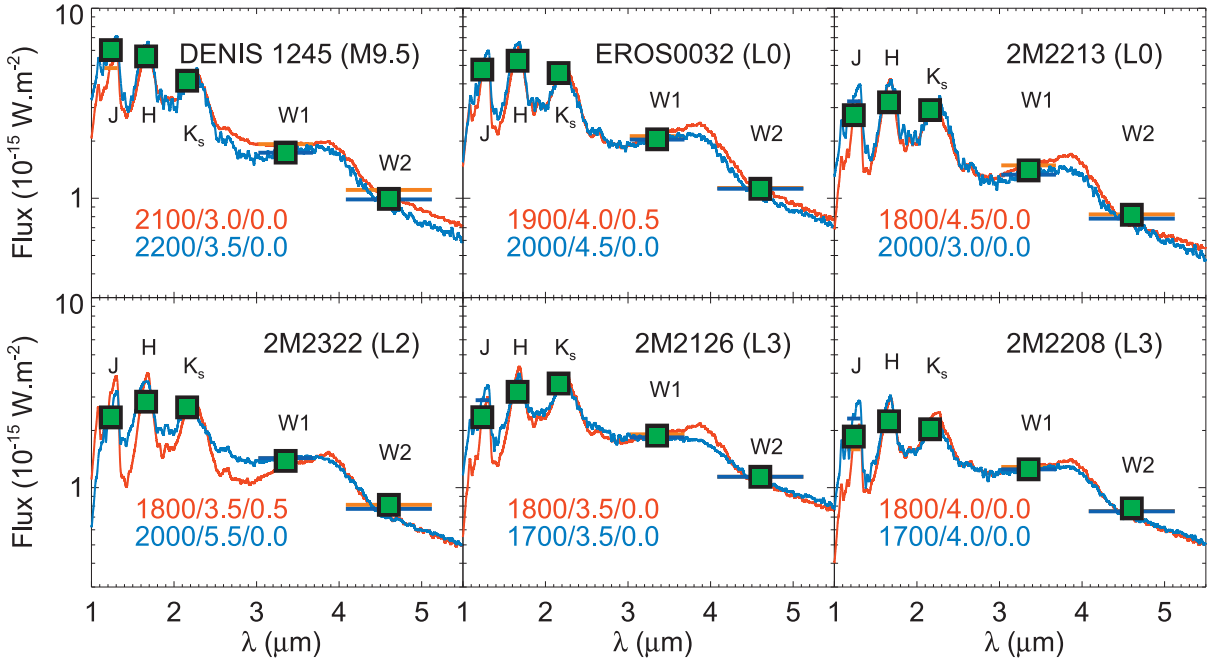

Fig. 12. Fit of the spectral energy distribution of five sources of the target sample (green squares) without noticeable excess emission by BT-Settl 2010 (blue) and BT-Settl 2013 (red) synthetic fluxes (laying bars). The corresponding best-fit spectra are overlaid.

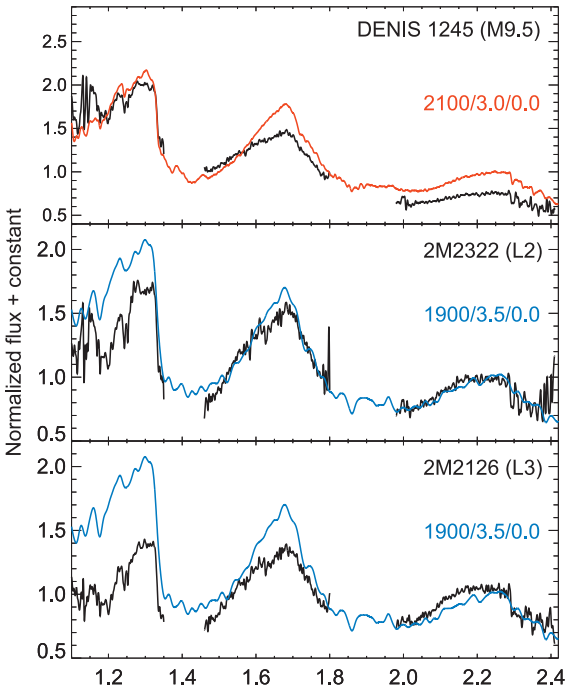

Fig. 13. ISAAC spectra (black) smoothed at $R = 300$ compared to best-fit BT-Settl 2010 (blue) and for BT-Settl 2013 (red) spectra with previously determined effective temperature inferred from the SED fit for objects for which an independent fit of the 1.1–2.5 μm does not yield the same effective temperature.

as if the 2013 solar metallicity models were not forming enough dust in the atmosphere compared to the 2010 models. This lack of dust could also explain why the models do not reproduce the shape of the pseudocontinuum in the H band well. The mismatch found in the BT-Settl 2010 models (Fig. 13) is also indicative of a lack of dust grains at high altitude/low optical depths in the cloud model. The problem may be solved with an ongoing revision of the models. The current version of the code uses a mixing length parameter (which parametrizes the vertical size of the convection cells) of 2 throughout the regime from M dwarfs to brown dwarfs. The new RHD simulations rather indicate that this parameter should be set to lower values. In addition, the grain growth in the 2013 models was artificially suppressed, as it was linked to the assumed availability of nucleation seeds. The next version of the models will treat growth by coagulation in a more consistent fashion and could, in principle, produce thicker clouds.

The fit of the SED is less influenced by localized errors in the models because of the extended spectral coverage and the lower resolution of the fit, set by the narrowest filter. If we assume that the SED fits are more reliable, we confirm the quick drop of the effective temperature at the M–L transition discovered for young optically-classified dwarfs (GSC 08047-00232 B, OTS 44, KPNO-Tau 4) by Bonnefoy et al. (2014a). The effective temperature remains nearly constant for the L0–L3γ dwarfs of the sample. These temperatures are close to those of other young L-type low-mass companions AB Pic b (Bonnefoy et al. 2010), 1RXS1609b (Lafrenière et al. 2008, 2010), GJ 417 B (Bonnefoy et al. 2014a), β Pictoris b (Bonnefoy et al. 2013), G196-3B (Zapatero Osorio et al. 2010), and CD-35 2722B (Wahhaj et al. 2011). This further suggests that β Pictoris b is an early-L dwarf.

5.2. Revised properties

We combine results from our analysis of the SED and the 1.1–2.5 μm ISAAC spectra to derive final estimates for the objects and we report them in Table 6. We prioritized the solutions derived from the SED fit with the BT-Settl 2013 models for the final estimate of the $T_{\rm eff}$. The values of the surface gravity correspond to the most frequent solutions found from the fit of the J, H, K, and JHK band spectra. The error bars were derived on a case-by-case basis from the dispersion of the atmospheric parameters.

Table 6. Adopted atmospheric parameters and bolometric luminosity.

Object	$T_{\rm eff}$ [K]	$\log g$	$\log_{10}(L/L_\odot)^a$
DENIS J1245	2200 ± 200	3.0 ± 0.5	−3.02 ± 0.21
EROS J0032	1900 ± 200	4.5 ± 0.5	−3.93 ± 0.11
2M 2203	1800 ± 100	4.0 ± 0.5	...
Cha 1305	1800 ± 100	4.0 ± 0.5	−3.13 ± 0.08
2M 2322	1800 ± 100	4.0 ± 0.5	...
2M 2126	1800 ± 100	4.0 ± 0.5	...
2M 2208	1800 ± 100	4.0 ± 0.5	...

Notes. [a] Recomputed based on the bolometric corrections of young M9.5 and L0 dwarfs reported in Todorov et al. (2010).

Table 7. Physical properties of the objects with known distance and age.

Object	Age (Myr)	M from $L/L_\odot{}^a$ ($M_{\rm Jup}$)	M from $T_{\rm eff}{}^a$ ($M_{\rm Jup}$)
DENIS 1245	10^{+10}_{-7}	16^{+19}_{-7}	16^{+9}_{-10}
Cha1305	4 ± 2	12^{+3}_{-4}	7 ± 2
EROS J0032	30^{+20}_{-10} ?	12 ± 2	13^{+15}_{-1}
EROS J0032	120 ± 20 ?	30 ± 6	33 ± 7
EROS J0032	21^{+4}_{-13}	11^{+1}_{-4}	13^{+2}_{-4}

Notes. [a] Derived from the evolutionary models of Chabrier et al. (2000).

These new parameters and complementary material found in the literature are used to rediscuss the properties of DENIS J1245, EROS J0032, Cha 1305, and 2M2213.

5.2.1. DENIS-P J124514.1-442907 (TWA 29)

The object DENIS-P J124514.1-442907 was identified as a probable member of the TW Hydrae association (Kastner et al. 1997) by Looper et al. (2007). Membership was initially based on estimated distance, sky position relative to known association members, proper-motions, Hα emission, and features indicative of low surface gravity in low-resolution ($R \sim 120$), NIR (0.94–2.5 μm) and medium-resolution ($R \sim 1800$), red-optical spectra of the source. Looper et al. derived spectral types M9.5 and M9pec, respectively, from their optical and near-infrared spectra. Manara et al. (2013) derived a comparable range of spectral types (M7.2–L0.8) by calculating spectral indices in an 0.58–2.4 μm medium-resolution ($R \sim 3500$) spectrum of DENIS J1245. These spectral type estimates are in agreement with our value (Table 3).

The membership of DENIS J1245 in the TW Hydrae association was revisited by both Schneider et al. (2012) and Weinberger et al. (2013). Schneider et al. used revised proper motion measurements to assess the membership in the context of other proposed members and found that membership was highlylikely, despite the lack of a measured parallax at the time. Weinberger et al. measured a parallax and new proper motions from dedicated, multi-epoch photometry and found that the the overall kinematics and Galactic position of the brown dwarf were consistent with the distribution of other higher-mass members of the association.

We used the online BANYAN tool of Malo et al. (2013) to calculate a membership probability based on the position, proper motion, and measured parallax. The Bayesian analysis provides a 95% probability of the brown dwarf being a member of the TW Hydrae association based only on the available kinematics (i.e., not considering the evidence for youth). We also use the methods of Lépine & Simon (2009) and Schlieder et al. (2010, 2012) to constrain group membership. We calculated ϕ, the angle between the source proper motion vector and that expected for the average motion of kinematic moving group members at its position, and $d_{\rm kin}$, the source's distance assuming it is a group member. We checked these values for each of the young, kinematic groups described in Torres et al. (2008). We found ϕ for DENIS J1245 was smallest when calculated for both the β Pictoris moving group and the TW Hydrae association, ~5.5°. This angle is typically $\lesssim$10° for well established group members. The $d_{\rm kin}$ predicted for both moving groups was also very similar, ~95 pc, and generally consistent with the 79 ± 13 pc distance measured by Weinberger et al. (2013). However, the Galactic *XYZ* distances of the brown dwarf are most consistent with other members the TW Hydrae association, particularly the positive *Z* distance. These results are consistent with previous kinematic studies, and when combined with previous evidence for youth and the spectral features indicative of verylow surface gravity in our ISAAC spectrum, indicate DENIS J1245 is a very strong candidate for TWA membership. Designation as a true member will require an accurate RV measurement.

Witte et al. (2011) compared their DRIFT-PHOENIX model spectra to the NIR spectrum of Looper et al. (2007) to derive $T_{\rm eff} = 1900$ K, $\log g = 4.5$ and [M/H] = 0.0. Our estimates of these physical parameters are consistent with these values if we consider a 100 K error on their measurements, corresponding to the sampling in effective temperature of their model template grid. Nevertheless, they disagree with the temperature derived from the fit of the 1.1–2.5 μm only. Our estimates of the effective temperature (from the SED, or the spectra) are in good agreement with the temperature ($T_{\rm eff} = 2300$ K) derived from the extension (Briceño et al. 2002) of the spectral type temperature conversion scale of Luhman (1999) and Luhman et al. (2003). We derive a mass of 16^{+9}_{-10} $M_{\rm Jup}$ for DENIS J1245 by comparing our temperature (reported in Table 6) to predictions of the DUSTY evolutionary models (Chabrier et al. 2000) for an age of 10^{+10}_{-7} Myr (Barrado y Navascués 2006).

We used the parallax measurement of Weinberger et al. (2013) and the BC_K for young M9.5 dwarfs derived by Todorov et al. (2010) to estimate the bolometric luminosity (Table 7) of the source. This luminosity corresponds to a predicted mass consistent with that derived from $T_{\rm eff}$ (see Table 7). We thus confirm that to date, DENIS J1245 is the lowest mass isolated object proposed to be a member of the TW Hydrae association. The semiempirical radius derived in Sect. 4.2 is consistent with evolutionary model predictions (Chabrier et al. 2000) for the estimated age of the object.

5.2.2. EROS-MP J0032-4405

The object EROS-MP J0032-4405 was discovered by Goldman et al. (1999). Martín et al. (1999) adopted a spectral type of L0 from the analysis of an optical spectrum and identified strong Li 6708 Å absorption. The detection of Li constrained the mass to $M \leq 50$ $M_{\rm Jup}$ and the age to be younger than ~0.5 Gyr. Goldman et al. (1999) used NG-Dusty models to estimate a temperature of $T_{\rm eff} = 1850 \pm 150$ K, comparable to our estimate from SED fitting. Cruz et al. (2009) classified this object as very-low gravity L0γ type and estimated a spectroscopic distance of $d_{\rm sp} = 41 \pm 5$ pc. Allers & Liu (2013) also presented a low-resolution NIR spectrum and used their index based methods to classify it as L0 VL-G (very low gravity). Accurate proper

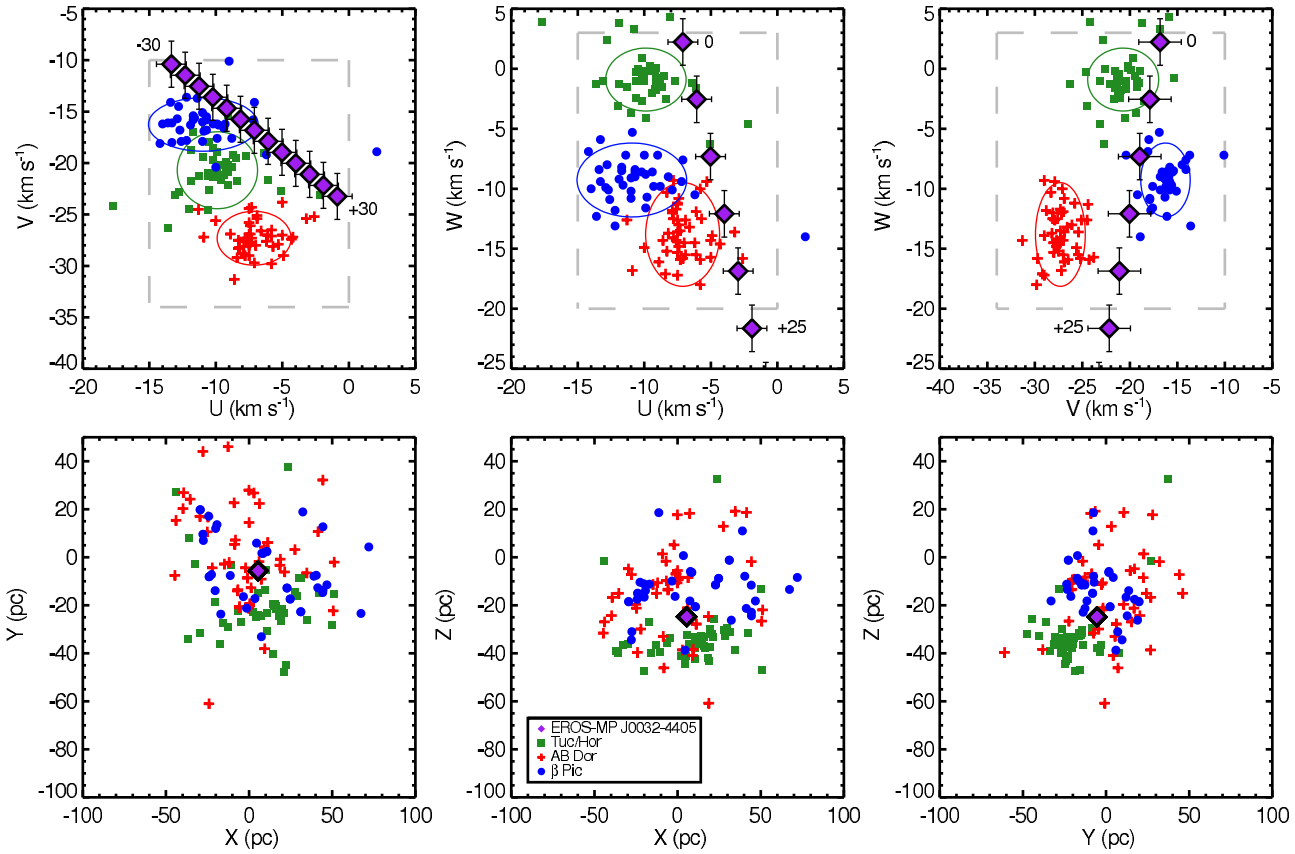

Fig. 14. Projections of the 6D Galactic kinematics of EROS J0032 compared to the young Tucana/Horologium, AB Doradus, and β Pictoris kinematic groups. EROS J0032 is presented by a violet diamond with associated error bars. The multiple points represent different possible values of the radial velocity (RV), ranging from –30 km s^{-1} to +30 km s^{-1} in increments of 5 km s^{-1}. The young kinematic groups are designated in the figure legend. *Top panels*: projections in (*UVW*) Galactic velocity. The colored ellipses designate the 2σ dispersion of the average velocities of each group from Malo et al. (2013). EROS J0032 is most consistent with the Tuc/Hor and β Pic groups for RVs between ~5 and 10 km s^{-1}. *Bottom panels*: projections of the (*XYZ*) Galactic distance. EROS J0032 is consistent with the distributions of all three young groups. For reference, we also plot the Galactic velocity space occupied by most young stars in the solar neighborhood as a dashed, grey box (Zuckerman & Song 2004).

motions and a parallax of 38.4 ± 4.8 mas were presented in Faherty et al. (2012).

Our index based analysis of our ISAAC spectrum provided a spectral type consistent with the L0 determined by Cruz et al. (2009) and Allers & Liu (2013). However, the gravity sensitive spectral features in our medium-resolution spectrum provide a slightly different view of the brown dwarf's age. Figures 5 and 6 show that the gravity sensitive K I lines and FeH band in the *J*-band and the shape of the *H*-band continuum are consistent with a surface gravity that is only slightly weaker than typical field brown dwarfs of similar spectra type. These features are more suggestive of an intermediate surface gravity and thus an older age than the previous optical and near-infrared spectra. Since our knowledge of how dust and low-surface gravity affect individual spectral features and overall spectral morphology at different wavelengths and spectral resolutions is incomplete, it is difficult to assess this discrepancy. As shown for two proposed L-type members of the AB Doradus moving group in Allers & Liu (2013), even the spectra of brown dwarfs at the same purported age and temperature exhibit features consistent with different surface gravities.

Cruz et al. (2009) showed that the sky position of EROS J0032 and many other young, field dwarfs were coincident with known members of young kinematic groups. To follow up these preliminary suggestions, we followed the same procedures as described for DENIS J1245 to investigate possible membership of EROS J0032 in kinematic moving groups. Using only the available proper motions and parallax, the Malo et al. (2013) online tool provides ~92% membership probability in the Tucana/Horologium association (Tuc/Hor), ~8% membership probability in the AB Doradus moving group (AB Dor), and <1% probability in the β Pictoris moving group (β Pic) and the field. However, the potential membership EROS J0032 in a young moving group hinges on its radial velocity (RV).

We illustrate this in Fig. 14, where we show projections of the six-dimensional Galactic kinematics[3] of EROS J0032 for a range of possible RVs ([–30, 30] km s^{-1}). The figure reveals that the kinematics of the brown dwarf are a relatively good match to both the Tuc/Hor and β Pic groups for RVs between ~5–10 km s^{-1}. The object EROS J0032 is also close to the AB Dor group distribution for RVs ~15–20 km s^{-1}, but remains a >4σ outlier in the (*UV*) plane. EROS J0032 is consistent with the (*XYZ*) of any of these groups. To complete the kinematic analysis, we also calculated ϕ = 5.3°, ϕ = 0.9°, ϕ = 19.5° when comparing the brown dwarf's proper motions to the Tuc/Hor, AB Dor, and β Pic groups, respectively. The $d_{\rm kin}$ calculated for

[3] *UVWXYZ*, where *U*, *V*, and *W* are Galactic velocities and *X*, *Y*, and *Z* are Galactic distances. *U* and *X* are positive toward the Galactic center, *V* and *Y* are positive in the direction of the Sun's motion around the Galaxy, and *W* and *Z* are positive toward the north Galactic pole. The sun lies at (*UVWXYZ*) = (0, 0, 0, 0, 0, 0).

the groups are also very comparable: 32 pc for Tuc/Hor, 37 pc for AB Dor, and 26 pc for β Pic. All of these distances are broadly consistent with the measured parallax distance of 26.0 ± 3.3 pc, but the match to β Pic is the best. Thus, we conclude that the kinematics of EROS J0032 are most suggestive of possible membership in either the Tuc/Hor or β Pic groups, but without a measured RV, definitive membership cannot be assigned.

For completeness, we estimate the mass of EROS J0032 by comparing our derived effective temperature to DUSTY evolutionary model predictions for two different age ranges: 20–40 Myr for possible Tuc/Hor or β Pic membership and 130 ± 20 Myr for possible AB Dor membership (Zuckerman et al. 2001; Barenfeld et al. 2013). If the brown dwarf is a member of β Pic, its mass is comparable to those of directly imaged planets (see Table 7).

5.2.3. Cha J130540.8-773958

Our new effective temperature determination for Cha J1305 falls in the same range as the temperatures of 1–3 Myr old M9.5–L0 objects OTS 44 (Luhman et al. 2004), KPNO Tau 4 (Briceño et al. 2002), and Cha J110913-773444 (Luhman et al. 2005). This is consistent with the observed similarities between the spectrum of OTS 44 and the low-resolution ($R \sim 300$) NIR spectrum of Cha 1305 presented by Allers et al. (2007). The optical spectral type (L0 ± 2) derived by Jayawardhana & Ivanov (2006) is also consistent with the NIR spectral type.

We recomputed the luminosity of Cha 1305 and report it in Table 7. This luminosity is based on the BC_K of young L0 dwarfs (Todorov et al. 2010), the K band magnitude of the source, corrected for an $A_V = 3$ mag (Allers et al. 2007; Spezzi et al. 2008), and an associated distance of 178 ± 18 pc for the Chameleon II star forming cloud (Whittet et al. 1997). We compared the temperature and luminosity of Cha J1305 to Chabrier et al. (2000) evolutionary tracks and retrieved a mass of 5–15 $M_{\rm Jup}$ for a Chameleon II age of 4 ± 2 Myr (Spezzi et al. 2008). This mass is consistent with the previous mass estimate presented by Allers et al. (2007).

5.2.4. 2MASS J22134491-2136079

2MASS J22134491-2136079 was identified as a peculiar L0 type object with probable low gravity features (Cruz et al. 2007). This gravity classification was based on the strength of VO bands and alkali doublets in the optical. However, Hα emission was not detected. Kirkpatrick et al. (2008) estimated an age of less than ∼100 Myr via visual comparison to the optical spectra of other brown dwarfs with known ages. Kirkpatrick et al. (2008) considered the estimated age and sky position of 2M 2213 to suggest that it is a possible member of the β Pictoris moving group. Cruz et al. (2009) estimated a distance of 54 ± 7 pc using the M_J–spectral type relation from Cruz et al. (2003). Allers & Liu (2013) classified 2M 2213 as spectral type L0 with very low surface gravity from a low-resolution ($R \sim 100$) IRTF/SpeX spectrum. This classification is at odds with the L2pec NIR spectral type of Marocco et al. (2013), likely because Marocco et al. (2013) only compare the spectrum of the source to those of mature field dwarfs.

We report here the first estimate of the temperature of the object using atmospheric models, and find atmospheric parameters that confirm the low surface gravity of the object. To further investigate possible young kinematic group membership, we use the proper motions measured by Faherty et al. (2009) to apply the same tests of group membership used for DENIS 1245 and EROS J0032. The BANYAN Bayesian analysis tool provides ambiguous probabilities for group membership: ∼30% β Pictoris, ∼20% Tuc/Hor, and ∼50% field. The angle ϕ is also <10° for many of the kinematic groups discussed in Torres et al. (2008). The photometric distance estimated by Cruz et al. (2009) could be used to potentially rule out membership in several groups, but a parallax measurement is preferred given the young age of 2M 2213. Thus, the currently available data do not allow for constraints on 2M 2213's possible kinematic group membership. The topic should be revisited once RV and parallax measurements are available for this young brown dwarf.

6. Conclusions

We obtained and analyzed seven VLT/ISAAC medium-resolution ($R \sim 1500$–1700) spectra of M9.5–L3 dwarfs classified at optical wavelengths and showing indications of low surface gravity. We built an age sequence of M9.5 objects that allow us to pinpoint age-sensitive and gravity-sensitive features at medium-resolving powers. The comparison of our spectra to those of young reference brown dwarfs and their companions, and of mature field dwarfs confirm that our objects have peculiar features in the NIR indicative of low surface gravities and young ages. We also confirm the youth of our objects by calculating the equivalent widths of their KI lines and comparing these values per spectral type with the values obtained for young reference brown dwarfs and companions and mature field dwarfs. We derived NIR spectral types based on dedicated spectral indices. These spectral types are in agreement with the optical classification, and confirm the coherence of the classification method. The analysis revealed that the L2γ object 2MASS J2322 provides a good match to the spectrum of the young planetary mass companion 1RXS J160929.1-210524b.

The spectra and SEDs of the objects can be reproduced by the 2010 and 2013 BT-Settl atmospheric models. The 2013 release of the models simultaneously fit the spectra and the SED for the same temperatures at all wavelengths. L0–L3γ dwarfs have nearly equal temperatures at around 1800 K. Nevertheless, we identify that:

- The 2010 models do not reproduce the 1.1–2.5 μm spectral slope of some L2–L3 objects.
- The H band shape is not well reproduced by the BT-Settl 2013 models at solar metallicity. The problem disappears when new, but not well-tested, models at super-solar metallicity are used, but these models remain mostly untested.

Currently, all these discrepancies point out a lack of dust in the cloud models. The next version of the BT-Settl models will modify the treatment of the vertical mixing and of grain growth processes. These new models are expected to produce thicker clouds, and may solve the issues revealed by the ISAAC spectra.

The spectra of the objects will help to confirm the membership of photometrically-selected candidates in star-forming regions. Within the next few years, surveys on the next generation of planet imaging instruments such as the Spectro-Polarimetric High-contrast Exoplanet REsearch (SPHERE) at VLT, the Gemini Planet Imager (GPI) at Gemini South, the *Subaru* Coronagraphic Extreme AO Project (ScEXAO) at *Subaru*, and the Large Binocular Telescope mid-infrared camera (LMIRCam) at LBT should provide a sample of a few dozen young companions. Several planets similar to β Pictoris b should be unearthed and fall in the same temperature range as our objects. Therefore, our spectra will serve as precious benchmarks

for the characterization of the physical and atmospheric properties of these companions.

Note added in proof. While this work was in peer review, Gagné et al. (2014) published a revised version of the BANYAN tool (BANYAN II) and presented a detailed analysis of two of our targets. Using BANYAN II, they found a 93.3% probability that DENIS-P J124514.1-442907 (TWA 29) is a member of the TW Hydrae association and a 91.8% probability that EROS-MP J0032-4405 is a member of the β Pictoris moving group. These new results are consistent with ours as presented in Sect. 5.2.

Acknowledgements. We are grateful to the ESO staff for their support during the preparation of the observations and their execution. We thank Emily Rice, Kathlyn Allers, Quinn Konopacky, Stan Metchev, David Lafrenière, Jenny Patience, Michael Liu, Tobias Schmidt, Andreas Seifahrt, Brendan Bowler, Zahed Wahhaj, Laird Close, Davy Kirkpatrick, Nadya Gorlova, Carlo Felice Manara, and Catherine Slesnick for providing the spectra of their low-gravity/young objects. We also thank Michael Cushing, John Rayner, and Ian Mc Lean for providing online access to their spectral librairies. This research has benefited from the SpeX Prism Spectral Libraries, maintained by Adam Burgasser at http://pono.ucsd.edu/~adam/browndwarfs/spexprism. It has also made use of the SIMBAD database operated at the CDS, Strasbourg, France. G. Chauvin, A.-M. Lagrange, F. Allard, and D. Homeier acknowledge financial support from the French National Research Agency (ANR) through project grant ANR10-BLANC0504-01. This project is also supported by the "Programme National de Physique Stellaire" (PNPS) of the CNRS (INSU) in France, the European Research Council under the European Community's Seventh Framework Program (FP7/2007-2013 Grant Agreement No. 247060), and the Lyon Institute of Origins under grant ANR-10-LABX-66. This work was supported by Sonderforschungsbereich SFB 881 "The Milky Way System" (subproject B6) of the German Research Foundation (DFG). N. Lodieu was funded by the Ramón y Cajal fellowship number 08-303-01-02. This research has been partially supported by the Spanish Ministry of Economics and Competitiveness under projects AYA2010-19136, Fondecyt #1120299 and Basal initiative PFB06.

References

Alcalá, J. M., Spezzi, L., Chapman, N., et al. 2008, ApJ, 676, 427
Allard, F., Hauschildt, P. H., Alexander, D. R., Tamanai, A., & Schweitzer, A. 2001, ApJ, 556, 357
Allard, F., Guillot, T., Ludwig, H.-G., et al. 2003a, in Brown Dwarfs, ed. E. Martín, IAU Symp., 211, 325
Allard, N. F., Allard, F., Hauschildt, P. H., Kielkopf, J. F., & Machin, L. 2003b, A&A, 411, L473
Allard, F., Allard, N. F., Homeier, D., et al. 2007, A&A, 474, L21
Allard, F., Homeier, D., & Freytag, B. 2011, in 16th Cambridge Workshop on Cool Stars, Stellar Systems, and the Sun, eds. C. Johns-Krull, M. K. Browning, & A. A. West, ASP Conf. Ser., 448, 91
Allard, F., Homeier, D., & Freytag, B. 2012a, R. Soc. London Phil. Trans. Ser. A, 370, 2765
Allard, F., Homeier, D., Freytag, B., & Sharp, C. M. 2012b, in EAS Publ. Ser. 57, eds. C. Reylé, C. Charbonnel, & M. Schultheis, 3
Allard, F., Homeier, D., Freytag, B., Schaffenberger, W., & Rajpurohit, A. S. 2013, Mem. Soc. Astron. It. Suppl., 24, 128
Allen, P. R., Koerner, D. W., McElwain, M. W., Cruz, K. L., & Reid, I. N. 2007, AJ, 133, 971
Allers, K. N., & Liu, M. C. 2007, in AAS Meeting Abstracts, 103.15, BAAS, 39, 921
Allers, K. N., & Liu, M. C. 2013, ApJ, 772, 79
Allers, K. N., Kessler-Silacci, J. E., Cieza, L. A., & Jaffe, D. T. 2006, ApJ, 644, 364
Allers, K. N., Jaffe, D. T., Luhman, K. L., et al. 2007, ApJ, 657, 511
Allers, K. N., Liu, M. C., Shkolnik, E., et al. 2009, ApJ, 697, 824
Allers, K. N., Liu, M. C., Dupuy, T. J., & Cushing, M. C. 2010, ApJ, 715, 561
Alves de Oliveira, C., Moraux, E., Bouvier, J., & Bouy, H. 2012, A&A, 539, A151
Asplund, M., Grevesse, N., Sauval, A. J., & Scott, P. 2009, ARA&A, 47, 481
Baraffe, I., Chabrier, G., Allard, F., & Hauschildt, P. H. 1998, A&A, 337, 403
Barber, R. J., Tennyson, J., Harris, G. J., & Tolchenov, R. N. 2006, MNRAS, 368, 1087
Barenfeld, S. A., Bubar, E. J., Mamajek, E. E., & Young, P. A. 2013, ApJ, 766, 6
Barman, T. S., Macintosh, B., Konopacky, Q. M., & Marois, C. 2011a, ApJ, 733, 65
Barman, T. S., Macintosh, B., Konopacky, Q. M., & Marois, C. 2011b, ApJ, 735, L39
Barrado y Navascués, D. 2006, A&A, 459, 511
Béjar, V. J. S., Zapatero Osorio, M. R., Pérez-Garrido, A., et al. 2008, ApJ, 673, L185
Bonnefoy, M., Chauvin, G., Rojo, P., et al. 2010, A&A, 512, A52
Bonnefoy, M., Boccaletti, A., Lagrange, A.-M., et al. 2013, A&A, 555, A107
Bonnefoy, M., Chauvin, G., Lagrange, A.-M., et al. 2014a, A&A, 562, A127
Bonnefoy, M., Currie, T., Marleau, G.-D., et al. 2014b, A&A, 562, A111
Borysow, A. 2002, A&A, 390, 779
Borysow, A., Jorgensen, U. G., & Zheng, C. 1997, A&A, 324, 185
Bowler, B. P., Liu, M. C., Kraus, A. L., Mann, A. W., & Ireland, M. J. 2011, ApJ, 743, 148
Bowler, B. P., Liu, M. C., Shkolnik, E. L., et al. 2012, ApJ, 753, 142
Bowler, B. P., Liu, M. C., Shkolnik, E. L., & Dupuy, T. J. 2013, ApJ, 774, 55
Briceño, C., Luhman, K. L., Hartmann, L., Stauffer, J. R., & Kirkpatrick, J. D. 2002, ApJ, 580, 317
Burgasser, A. J., Kirkpatrick, J. D., Brown, M. E., et al. 2002, ApJ, 564, 421
Burrows, A., & Sharp, C. M. 1999, ApJ, 512, 843
Burrows, A., Marley, M., Hubbard, W. B., et al. 1997, ApJ, 491, 856
Burrows, A., Hubbard, W. B., Lunine, J. I., & Liebert, J. 2001, Rev. Mod. Phys., 73, 719
Caffau, E., Ludwig, H.-G., Steffen, M., Freytag, B., & Bonifacio, P. 2011, Sol. Phys., 268, 255
Chabrier, G., Baraffe, I., Allard, F., & Hauschildt, P. 2000, ApJ, 542, 464
Chauvin, G., Lagrange, A.-M., Dumas, C., et al. 2004, A&A, 425, L29
Chauvin, G., Lagrange, A.-M., Zuckerman, B., et al. 2005, A&A, 438, L29
Close, L. M., Thatte, N., Nielsen, E. L., et al. 2007, ApJ, 665, 736
Cohen, M., Wheaton, W. A., & Megeath, S. T. 2003, AJ, 126, 1090
Cruz, K. L., Reid, I. N., Liebert, J., Kirkpatrick, J. D., & Lowrance, P. J. 2003, AJ, 126, 2421
Cruz, K. L., Faherty, J., Kirkpatrick, D., & Burgasser, A. J. 2007, in AAS Meeting Abstracts #210, BAAS, 39, 225
Cruz, K. L., Kirkpatrick, J. D., & Burgasser, A. J. 2009, AJ, 137, 3345
Currie, T., Daemgen, S., Debes, J., et al. 2014, ApJ, 780, L30
Cushing, M. C., Rayner, J. T., & Vacca, W. D. 2005, ApJ, 623, 1115
Cutri, R. M., et al. 2012, VizieR Online Data Catalog: II/311
Cutri, R. M., Skrutskie, M. F., van Dyk, S., et al. 2003, VizieR Online Data Catalog: II/246
Delorme, P., Gagné, J., Girard, J. H., et al. 2013, A&A, 553, L5
Devillard, N., Jung, Y., & Cuby, J.-G. 1999, The Messenger, 95, 5
Dulick, M., Bauschlicher, Jr., C. W., Burrows, A., et al. 2003, ApJ, 594, 651
Faherty, J. K., Burgasser, A. J., Cruz, K. L., et al. 2009, AJ, 137, 1
Faherty, J. K., Burgasser, A. J., Walter, F. M., et al. 2012, ApJ, 752, 56
Faherty, J. K., Rice, E. L., Cruz, K. L., Mamajek, E. E., & Núñez, A. 2013, AJ, 145, 2
Fitzpatrick, E. L. 1999, PASP, 111, 63
Freytag, B., Allard, F., Ludwig, H.-G., Homeier, D., & Steffen, M. 2010, A&A, 513, A19
Freytag, B., Steffen, M., Ludwig, H.-G., et al. 2012, J. Comput. Phys., 231, 919
Gagné, J., Lafrenière, D., Doyon, R., Malo, L., & Artigau, É. 2014, ApJ, 783, 121
Geballe, T. R., Knapp, G. R., Leggett, S. K., et al. 2002, ApJ, 564, 466
Goldman, B., Delfosse, X., Forveille, T., et al. 1999, A&A, 351, L5
Gorlova, N. I., Meyer, M. R., Rieke, G. H., & Liebert, J. 2003, ApJ, 593, 1074
Hayes, D. S. 1985, in Calibration of Fundamental Stellar Quantities, eds. D. S. Hayes, L. E. Pasinetti, & A. G. D. Philip, IAU Symp., 111, 225
Helling, C., Dehn, M., Woitke, P., & Hauschildt, P. H. 2008, ApJ, 675, L105
Ireland, M. J., Kraus, A., Martinache, F., Law, N., & Hillenbrand, L. A. 2011, ApJ, 726, 113
Jarrett, T. H., Cohen, M., Masci, F., et al. 2011, ApJ, 735, 112
Jayawardhana, R., & Ivanov, V. D. 2006, ApJ, 647, L167
Kastner, J. H., Zuckerman, B., Weintraub, D. A., & Forveille, T. 1997, Science, 277, 67
Kirkpatrick, J. D. 2005, ARA&A, 43, 195
Kirkpatrick, J. D., Reid, I. N., Liebert, J., et al. 1999, ApJ, 519, 802
Kirkpatrick, J. D., Dahn, C. C., Monet, D. G., et al. 2001, AJ, 121, 3235
Kirkpatrick, J. D., Barman, T. S., Burgasser, A. J., et al. 2006, ApJ, 639, 1120
Kirkpatrick, J. D., Cruz, K. L., Barman, T. S., et al. 2008, ApJ, 689, 1295
Kirkpatrick, J. D., Looper, D. L., Burgasser, A. J., et al. 2010, ApJS, 190, 100
Konopacky, Q. M., Barman, T. S., Macintosh, B. A., & Marois, C. 2013, Science, 339, 1398
Kuzuhara, M., Tamura, M., Kudo, T., et al. 2013, ApJ, 774, 11
Lafrenière, D., Jayawardhana, R., & van Kerkwijk, M. H. 2008, ApJ, 689, L153
Lafrenière, D., Jayawardhana, R., & van Kerkwijk, M. H. 2010, ApJ, 719, 497
Lagrange, A.-M., Bonnefoy, M., Chauvin, G., et al. 2010, Science, 329, 57

Lavigne, J.-F., Doyon, R., Lafrenière, D., Marois, C., & Barman, T. 2009, ApJ, 704, 1098
Lépine, S., & Simon, M. 2009, AJ, 137, 3632
Liu, M. C., Magnier, E. A., Deacon, N. R., et al. 2013, ApJ, 777, L20
Lodders, K. 1999, ApJ, 519, 793
Lodieu, N., Hambly, N. C., Jameson, R. F., & Hodgkin, S. T. 2008, MNRAS, 383, 1385
Looper, D. L., Burgasser, A. J., Kirkpatrick, J. D., & Swift, B. J. 2007, ApJ, 669, L97
Looper, D. L., Kirkpatrick, J. D., Cutri, R. M., et al. 2008, ApJ, 686, 528
Lucas, P. W., Roche, P. F., Allard, F., & Hauschildt, P. H. 2001, MNRAS, 326, 695
Ludwig, H.-G., Allard, F., & Hauschildt, P. H. 2002, A&A, 395, 99
Ludwig, H.-G., Allard, F., & Hauschildt, P. H. 2006, A&A, 459, 599
Luhman, K. L. 1999, ApJ, 525, 466
Luhman, K. L. 2004, ApJ, 617, 1216
Luhman, K. L., Liebert, J., & Rieke, G. H. 1997, ApJ, 489, L165
Luhman, K. L., Stauffer, J. R., Muench, A. A., et al. 2003, ApJ, 593, 1093
Luhman, K. L., Peterson, D. E., & Megeath, S. T. 2004, ApJ, 617, 565
Luhman, K. L., Adame, L., D'Alessio, P., et al. 2005, ApJ, 635, L93
Luhman, K. L., Patten, B. M., Marengo, M., et al. 2007, ApJ, 654, 570
Lunine, J. I., Hubbard, W. B., & Marley, M. S. 1986, ApJ, 310, 238
Malo, L., Doyon, R., Lafrenière, D., et al. 2013, ApJ, 762, 88
Manara, C. F., Testi, L., Rigliaco, E., et al. 2013, A&A, 551, A107
Marley, M. 2000, in From Giant Planets to Cool Stars, eds. C. A. Griffith & M. S. Marley, ASP Conf. Ser., 212, 152
Marley, M. S., & Ackerman, A. S. 2001, ApJ, in press [arXiv:astro-ph/0103269]
Marley, M. S., Saumon, D., Cushing, M., et al. 2012, ApJ, 754, 135
Marley, M. S., Ackerman, A. S., Cuzzi, J. N., & Kitzmann, D. 2013, In Comparative Climatology of Terrestrial Planets, eds. S.J. Mackwell, et al. (Tucson: Univ. of Arizona Press), 367
Marocco, F., Andrei, A. H., Smart, R. L., et al. 2013, AJ, 146, 161
Marois, C., Macintosh, B., Barman, T., et al. 2008, Science, 322, 1348
Marois, C., Zuckerman, B., Konopacky, Q. M., Macintosh, B., & Barman, T. 2010, Nature, 468, 1080
Martín, E. L., Delfosse, X., Basri, G., et al. 1999, AJ, 118, 2466
Martín, E. L., Delfosse, X., & Guieu, S. 2004, AJ, 127, 449
McGovern, M. R., Kirkpatrick, J. D., McLean, I. S., et al. 2004, ApJ, 600, 1020
McLean, I. S., McGovern, M. R., Burgasser, A. J., et al. 2003, ApJ, 596, 561
Metchev, S. A., & Hillenbrand, L. A. 2006, ApJ, 651, 1166
Mohanty, S., Jayawardhana, R., Huélamo, N., & Mamajek, E. 2007, ApJ, 657, 1064
Moorwood, A., Cuby, J.-G., Biereichel, P., et al. 1998, The Messenger, 94, 7
Mountain, C. M., Selby, M. J., Leggett, S. K., Blackwell, D. E., & Petford, A. D. 1985, A&A, 151, 399
Nakajima, T., Oppenheimer, B. R., Kulkarni, S. R., et al. 1995, Nature, 378, 463
Oasa, Y., Tamura, M., & Sugitani, K. 1999, ApJ, 526, 336
Oppenheimer, B. R., Baranec, C., Beichman, C., et al. 2013, ApJ, 768, 24
Patience, J., King, R. R., De Rosa, R. J., & Marois, C. 2010, A&A, 517, A76
Patience, J., King, R. R., De Rosa, R. J., et al. 2012, A&A, 540, A85
Pecaut, M. J., Mamajek, E. E., & Bubar, E. J. 2012, ApJ, 746, 154
Plez, B. 1998, A&A, 337, 495
Preibisch, T., & Zinnecker, H. 1999, AJ, 117, 2381
Rameau, J., Chauvin, G., Lagrange, A.-M., et al. 2013, ApJ, 772, L15
Rayner, J. T., Cushing, M. C., & Vacca, W. D. 2009, ApJS, 185, 289
Rebolo, R., Zapatero Osorio, M. R., & Martín, E. L. 1995, Nature, 377, 129
Rebolo, R., Zapatero Osorio, M. R., Madruga, S., et al. 1998, Science, 282, 1309
Reid, I. N., Kirkpatrick, J. D., Gizis, J. E., et al. 2000, AJ, 119, 369
Reid, I. N., Cruz, K. L., Kirkpatrick, J. D., et al. 2008, AJ, 136, 1290
Rice, E. L., Barman, T., Mclean, I. S., Prato, L., & Kirkpatrick, J. D. 2010, ApJS, 186, 63
Rossow, W. B. 1978, Icarus, 36, 1
Ruiz, M. T., Leggett, S. K., & Allard, F. 1997, ApJ, 491, L107
Schlieder, J. E., Lépine, S., & Simon, M. 2010, AJ, 140, 119
Schlieder, J. E., Lépine, S., & Simon, M. 2012, AJ, 143, 80
Schneider, A., Melis, C., & Song, I. 2012, ApJ, 754, 39
Seifahrt, A., Neuhäuser, R., & Hauschildt, P. H. 2007, A&A, 463, 309
Sembach, K. R., & Savage, B. D. 1992, ApJS, 83, 147
Silva, D. R., & Peron, M. 2004, The Messenger, 118, 2
Skemer, A. J., Hinz, P. M., Esposito, S., et al. 2012, ApJ, 753, 14
Slesnick, C. L., Hillenbrand, L. A., & Carpenter, J. M. 2004, ApJ, 610, 1045
Slesnick, C. L., Hillenbrand, L. A., & Carpenter, J. M. 2008, ApJ, 688, 377
Spezzi, L., Alcalá, J. M., Covino, E., et al. 2008, ApJ, 680, 1295
Tanaka, H. K. M. 2005, J. Atmos. Sol.-Terr. Phys., 67, 1544
Testi, L. 2009, A&A, 503, 639
Theodossiou, E., & Danezis, E. 1991, Ap&SS, 183, 91
Todorov, K., Luhman, K. L., & McLeod, K. K. 2010, ApJ, 714, L84
Torres, C. A. O., Quast, G. R., Melo, C. H. F., & Sterzik, M. F. 2008, in Handbook of Star Forming Regions, II, Vol. 5 (Southern Sky ASP Monograph Publications), 757
Tsuji, T., Ohnaka, K., Aoki, W., & Nakajima, T. 1996, A&A, 308, L29
Wahhaj, Z., Liu, M. C., Biller, B. A., et al. 2011, ApJ, 729, 139
Weck, P. F., Schweitzer, A., Stancil, P. C., Hauschildt, P. H., & Kirby, K. 2003, ApJ, 582, 1059
Weights, D. J., Lucas, P. W., Roche, P. F., Pinfield, D. J., & Riddick, F. 2009, MNRAS, 392, 817
Weinberger, A. J., Anglada-Escudé, G., & Boss, A. P. 2013, ApJ, 762, 118
Whittet, D. C. B., Prusti, T., Franco, G. A. P., et al. 1997, A&A, 327, 1194
Witte, S., Helling, C., Barman, T., Heidrich, N., & Hauschildt, P. H. 2011, A&A, 529, A44
Zapatero Osorio, M. R., Béjar, V. J. S., Martín, E. L., et al. 2000, Science, 290, 103
Zapatero Osorio, M. R., Rebolo, R., Bihain, G., et al. 2010, ApJ, 715, 1408
Zuckerman, B., & Song, I. 2004, ARA&A, 42, 685
Zuckerman, B., Song, I., & Webb, R. A. 2001, ApJ, 559, 388

Pages 20 to 21 are available in the electronic edition of the journal at http://www.aanda.org

Appendix A: Properties of the spectra of young companions

We summarize in Table A.1 the main characteristics of the spectra of young companions found in the literature and used in our empirical analysis. We did not report proposed spectral classes for these companions given the inhomogeneous classification scheme adopted in the literature.

Table A.1. Characteristics of the young companions spectra.

Name	Age (Myr)	λ_{min} (μm)	λ_{max} (μm)	R	Reference
2MASS J12073346-3932539 A	8	1.1	2.5	1500–2000	1
AB Pic b	30	1.1	2.5	1500–2000	1, 2
CT Cha b	1–3	1.1	2.5	1500–2000	1
DH Tau b	1–3	1.1	2.5	1500–2000	1
Gl 417 B	80–250	1.1	2.5	1500–2000	1
GSC 08047-00232 B	30	1.1	2.5	1500–2000	1
HR7329 B	12	1.1	2.5	1500–2000	1
TWA 5B	8	1.1	2.5	1500–2000	1
TWA 22A	12	1.1	2.5	1500–2000	1
TWA 22B	12	1.1	2.5	1500–2000	1
USCO CTIO 108B	3–11	1.1	2.5	1500–2000	1
1RXS J235133.3+312720 B	50–150	0.8	2.5	250–1200	3
2MASS J01225093-2439505 B	10–120	1.48	2.38	3800	4
GSC 06214-00210 b	3–11	1.1	1.8	3800	5
HD203030 b	130–400	2.0	2.6	2000	6
1RXS J160929.1-210524 b	3–11	1.15	2.4	6000–1300	7, 8
2MASS J12073346-3932539 b	8	1.1	2.5	1500–2000	9
CD-35 2722 B	100	1.15	2.40	5000–6000	10
G196-3B	100	1.1	2.4	2000	11
GQ Lup b	1–3	1.1	2.5	2000–4000	12
GQ Lup b	1–3	1.164	2.4	5000	13
HN Peg b	100–500	0.65	2.56	75	14
HR8799 b	30	1.48	2.36	60	15
HR8799 c	30	1.965	2.381	4000	16
SDSSJ224953.47+004404.6AB	100	0.8	2.5	150	17
TWA 8B	8	0.8	2.42	2000	11
TWA 11C	8	0.95	2.42	2000	11
AB Dor C	75–175	1.48	2.5	1500	18

References. 1) Bonnefoy et al. (2014a); 2) Bonnefoy et al. (2010); 3) Bowler et al. (2012); 4) Bowler et al. (2013); 5) Bowler et al. (2011); 6) Metchev & Hillenbrand (2006); 7) Lafrenière et al. (2008); 8) Lafrenière et al. (2010); 9) Patience et al. (2010); 10) Wahhaj et al. (2011); 11) Allers & Liu (2013); 12) Seifahrt et al. (2007); 13) Lavigne et al. (2009); 14) Luhman et al. (2007); 15) Barman et al. (2011a); 16) Konopacky et al. (2013); 17) Allers et al. (2010); 18) Close et al. (2007).

Appendix B: Best matches of EROS J0032, 2M 2213, 2M 2126, and 2M 2208 with library spectra

We present the result of the best matches after performing the empirical comparison of EROS J0032, 2M 2213, 2M 2126, and 2M 2208 spectra with library spectra in Sect. 3.2.

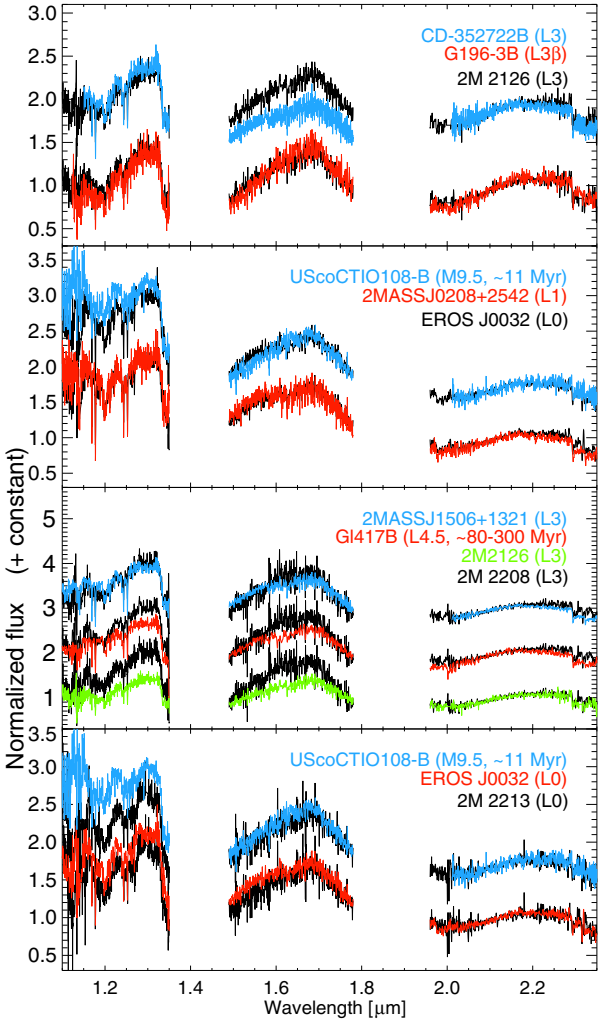

Fig. B.1. Best matches of the 1.1–2.38 μm spectra of EROS J0032, 2M 2213, 2M 2126, and 2M 2208 with library spectra.

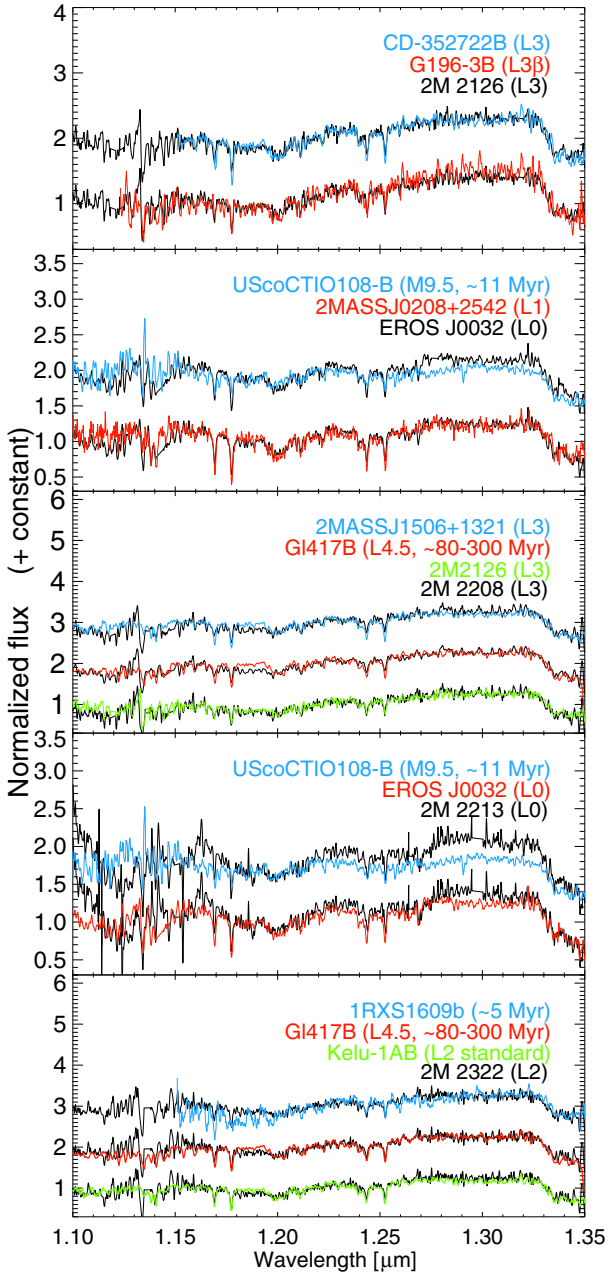

Fig. B.2. *J* band of best matches of the spectra of EROS J0032, 2M 2213, 2M 2126, and 2M 2208 with library spectra.